# Parametric excitation and friction modulation for a forced 2-DOF system

Sulollari, Enxhi; van Dalen, Karel; Cabboi, Alessandro

**DOI**
10.1007/s11071-024-10844-z

**Publication date**
2025

**Document Version**
Final published version

**Published in**
Nonlinear Dynamics

Nonlinear Dyn
https://doi.org/10.1007/s11071-024-10844-z

RESEARCH

# Parametric excitation and friction modulation for a forced 2-DOF system

**Enxhi Sulollari · Karel N. van Dalen · Alessandro Cabboi**

Received: 14 July 2024 / Accepted: 26 December 2024


**Abstract** A two degree of freedom mass on a moving belt system has been considered to study the effect of friction-induced oscillations, due to nonlinear contact properties and external excitation, on friction modulation. Both tangential and normal excitation are present and the Hertz-Damp model governs the normal contact. The combined presence of the normal-tangential coupling through friction and of the external excitation, results in a parametric excitation and triggers friction-induced oscillations. Using a numerical analysis, the occurrence of such oscillations is explained through the inspection of the friction force versus relative velocity plots, which indicate the presence of a negative damping effect in the tangential direction, despite considering Amontons-Coulomb law. Hence, a linearized stability analysis of the steady sliding state, by taking advantage of the Method of Direct Separation of Motion, is employed to predict the bifurcation point as function of system parameters. It is shown that the linearized stability analysis provides a good qualitative agreement for the occurrence of the friction-induced oscillations for the investigated system, while the quantitative match varies depending on the system parameters and their values. Lastly, the effect of the observed friction-induced oscillations on the friction modulation is studied. Through a numerical analysis, a significant degree of scatteredness in friction force modulation is observed. Such scatteredness is significantly linked to the emergence of friction-induced oscillations, and it also depends on the averaging procedure used to quantify the effective friction reduction.

**Keywords** Nonlinear contact · Friction-induced oscillations · Nonlinear vibration · Effective friction · Negative damping

E. Sulollari (✉) · K. N. van Dalen · A. Cabboi
Department of Engineering Structures, Faculty of Civil Engineering and GeoSciences, Delft University of Technology, Stevinweg 1, 2628CN Delft, The Netherlands
e-mail: E.Sulollari@tudelft.nl

K. N. van Dalen
e-mail: K.N.vanDalen@tudelft.nl

A. Cabboi
e-mail: A.Cabboi@tudelft.nl

## 1 Introduction

Friction-induced oscillations are very common in mechanical systems, and in most cases they are undesirable. Examples include the noise generated by door hinges or car brakes, and the chatter of machine tools or vibrations in slides and seals. One of the most studied mechanisms that leads to friction-induced oscillations is based on the presence of a decreasing friction force or friction coefficient linked to the corresponding increase in relative sliding velocity, naturally triggering a negative damping-like effect [1]. If such "negative damping" is higher than the bulk or structural damping of the system, instability occurs, characterized by the growth of the oscillatory motion during sliding. Friction-induced oscillations may also occur for a con-

Published online: 09 January 2025

stant value of the friction coefficient if phenomena such as sprag-slip [2–4] or mode coupling [5–8] characterize the system dynamics. Another mechanism that causes instability is the presence of a follower force for structures resembling the Pflüger or Ziegler column [9].

The role of damping is generally a key factor in friction-induced vibrations. In fact, with reference to the mode-coupling mechanism, Hoffmann and Gaul [5] analyzed a mass on belt system characterized by a vertical and horizontal degree of freedom, and concluded that the presence of non-proportional damping may, counterintuitively, destabilize the system. Similar observations were made by Sinou and Jezequel [6], pointing out that an optimal structural damping ratio and a pulsation ratio are capable of decreasing the unstable region due to mode coupling. Massi and Giannini [10] performed an experimental investigation of the relationship between the distribution of modal damping and the propensity to develop squeal in a beam-on-disk setup. Fritz and coworkers [11] used a finite element model of a whole brake corner and then a stability analysis to study the effects of damping on brake squeal coalescence patterns. Charroyer and coworkers [12] considered a mass-spring system of three degrees of freedom with friction and carried out parametric studies to evaluate the effects of various system parameters on stability, especially that of damping in mode-coupling instabilities with planar and rectilinear friction assumptions. Besides damping, the presence of a nonlinear contact stiffness has also a leading role in determining unstable regions. Li and coworkers [7] showed that an increase in the nonlinear stiffness, tends to destabilize the nonlinear system, while at certain higher values, a stable regime can be achieved.

Besides mechanisms leading towards friction-induced oscillations, techniques were also developed to mitigate such phenomena. Thomsen [13], for example, considered a mass-on-moving belt system subjected to a high-frequency tangential excitation and showed that the excitation can effectively cancel the negative slope in the friction-velocity relationship, thus preventing self-excited oscillations. Hoffman and coworkers [14] showed that external excitation has a stabilizing effect on the mode-coupling instability of a two degree of freedom model. Michaux and coworkers [15] studied the effect of the tangential excitation on the system stability considering the traditional mass-on-moving belt system and using a monotonic and a non-monotonic friction-velocity relations. Their study demonstrated that while excitation is found to always have a stabilizing influence in the case of a Stribeck friction law (non-monotonic friction-velocity relation), the system with the monotonic decreasing friction behaviour can be either stabilised or destabilised by the external excitation. The latter scenario, was already stressed out by Berger and coworkers [16,17], highlighting that the presence of excitation can also produce locally unstable responses. They considered a two degree of freedom system with linear contact properties, excited by the fluctuations caused by a rough surface while the tangential direction is excited by the normal-tangential coupling of friction. Arising from the velocity-dependent coupling of the normal and tangential modes and the periodic normal force variations, a parametric resonance was encountered for a ratio between forcing excitation and natural frequency in the normal direction equal to two.

The application of an external excitation has an effect not only on the system stability but also on the friction force, resulting into a friction modulation. In most studies, the effect of an oscillatory load on the friction force has been investigated with an emphasis on the high-frequency forcing [13–15]. Recently, Sulollari and coworkers [18] showed that the combination of the averaging technique and the velocity response function can be used to determine the vibration-induced effect on the friction force for a general frequency of excitation. Other than theoretical studies, several experimental studies on the influence of oscillatory loads on friction have been conducted. In the ’60 s, Tolstoi [19] showed experimentally that contact micro-vibrations, acting normal to the sliding plane, strongly affect both the magnitude of the frictional force and the stability of sliding. Later on, Tworzydlo and Becker [20], followed the general line of Tolstoi’s experiments and performed a numerical analysis assuming a non-linear normal compliance of the interface, matching the experimental data with a good accuracy. Matunaga and Onoda [21] also investigated the effect of vibration on the friction force, by means of a mass sliding on an in-plane vibrating table. The observed reduction of the friction force, due to oscillatory loads, was also predicted by a simplified model assuming Amontons-Coulomb law. Despite the qualitative match between experiments and model, the measured reduced friction force values also exhibited a non-negligible degree of scatteredness with reference to the analytical results. The reason for such discrepancy could be due to the omission

of system dynamic effects in the theoretical analysis. In later studies, the effect of the contact compliance on the vibration-induced friction modulation mechanism received more attention. For example, Kapelke and Seemann [22], adopted an elasto-plastic friction model (Dupont model [23]) to match their experimental results on friction modulation. However, the friction model parameters needed to be retuned, depending on the excitation frequency used. More recent studies [24,25] confirmed the need to use a compliant contact model to match experimental results of vibration-induced friction reduction, between various material pairs (e.g. steel, Teflon, PTFE) characterized by different surface roughness. In most of the investigation encountered so far, aimed at quantifying the vibration-induced friction modulation (or reduction) from experiments, an analysis on the stability of the investigated system is often missing.

With reference to the aforementioned background, the aim of this study is to analyze the stability of the continuous sliding state and the friction modulation of a two-degrees-of-freedom mass on belt system. The investigated system is governed by nonlinear contact properties and is harmonically excited in both the tangential and normal direction. The nonlinear contact is characterized by a normal contact force, which is assumed to be governed by the Hertz-Damp model [26]. The nonlinear normal force is then used to define the friction force which is proportional to a given coefficient of friction. The presence of a harmonic normal excitation and the normal-tangential coupling through friction results in a periodically time-varying dissipative term, representing parametric excitation. Contrary to what shown in [13–15], the numerical simulations highlight that occurrence of such parametric excitation along the tangential direction can destabilize an otherwise stable steady sliding state of the system. To complement and extend the results presented in [16,17], it is shown that the parametric excitation in the dissipative term leads to negative slopes in the friction force versus relative velocities relationship, indicating the presence of a negative damping mechanism which can trigger friction-induced vibrations, independently of the ratio between forcing excitation and natural frequencies of the system. Due to such instability mechanism, the harmonically excited system then oscillates not only at the excitation frequency but also at the natural frequency of the tangential mode. An attempt is made to predict the onset of such friction-induced vibrations through a linearized stability analysis, and taking advantage of the Method of Direct Separation of Motion [18,27,28] that allows to incorporate the averaged effects of the friction force. Through a brief numerical validation study, it is demonstrated that, for the investigated model configuration, the results from the linearized stability analysis show a good qualitative agreement with the occurrence of friction-induced oscillations, though the quantitative match varied depending on the system parameters and their values. Further numerical analysis also demonstrates how the occurrence of a friction-induced oscillation can drastically change the outcome of a friction modulation analysis. A significant degree of scatteredness in terms of friction force modulation is observed in the numerical results, mirroring those attained experimentally by Matunaga and Onoda [21] and depending on the averaging procedure used to quantify friction change. Averaging over the vibration period of the tangential mode results in almost no scatteredness.

In this paper, first the two-degree-of-freedom model with nonlinear contact properties is introduced in Sect. 2. In Sect. 3, friction-induced vibrations are observed through a numerical analysis and the mechanism triggering these vibrations is found. In Sect. 4, a stability analysis is performed where the eigenvalues of the Jacobian matrix of the linearized harmonically unforced and forced systems are calculated and the Routh-Hurwitz criteria is used to study the influence of system properties and excitation on the stability of the steady sliding state. In Sect. 5, the effect of these vibrations on friction modulation is portrayed. Finally, conclusions are drawn in Sect. 6 and Appendices are added, providing additional details to the discussions and to the results presented in this study.

## 2 The model system

To reveal the effects of system parameters and external excitation on the occurrence of friction-induced vibration and on friction change, the system illustrated in Fig. 1 is developed from a classic two-degree-of-freedom (2-DOF) model. The system consists of a mass $M$ positioned on a belt, moving at a constant speed $V_b$. In the tangential direction, a linear spring with stiffness $K_1$ and a linear dashpot with damping coefficient $C_1$ are present.

In the vertical direction, the Hertz-Damp contact model is employed [26], whereby a non-linear damper

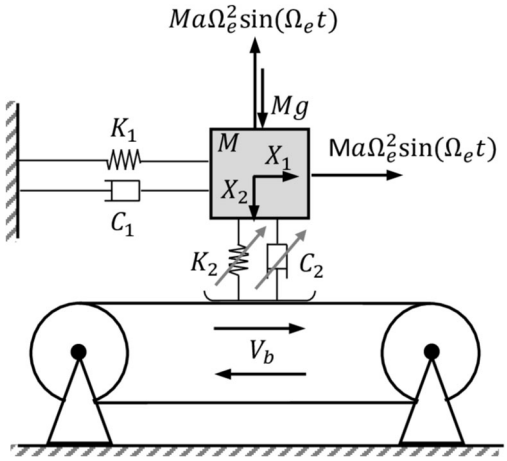


**Fig. 1** Layout of the 2-DOF Hetz-Damp system subject to external harmonic loads in the normal and tangential directions

is used in parallel with the Hertz spring [29]. According to this model, the normal force $F_n$ becomes:

$$F_n = \begin{cases} K_2 X_2^{3/2} + C_2 X_2^{3/2}\dot{X}_2 & \text{for} X_2 > 0 \\ 0 & \text{for} X_2 \leq 0, \end{cases} \quad (1)$$

where the stiffness $\frac{3}{2}K_2 X_2^{1/2}$ and the damping coefficient $C_2 X_2^{3/2}$ are respectively considered as the normal nonlinear contact stiffness and the nonlinear damping between the objects in relative sliding motion. Note that the use of the Hertz-Damp model for this study is not dictated by any specific application, but it only serves the purpose of introducing nonlinear terms in the normal direction. For the current study, nonlinear terms related to the tangential contact stiffness are neglected, since a high-level of complexity already arises due to the Hertz-Damp model. To avoid further complexities, the study of the transition between stick and slip through partial slip (see [30,31]) is also omitted. Throughout the study, and with reference to the stability analysis, only the continuous-sliding regime is considered. While stick–slip may still occur at certain belt velocities, the presence of an external excitation (especially in the horizontal direction) extends the range of velocities where continuous sliding takes place [13,14]. Additionally, as one of the key objectives of the study is to examine friction modulation, which is calculated by averaging the friction force over one oscillation period during sliding, on the case of stick–slip, this averaging approach is rather questionable, as it involves averaging a "static" and an oscillatory responses of the system. Furthermore, throughout the paper, the chosen system parameter values guarantee that the mass is always in contact with the belt (non-jumping condition).

Given the time-varying normal force, the expression of the friction force $F_f$ then becomes

$$F_f = \mu(V_r)F_n = \mu(V_r)(C_2 X_2^{3/2}\dot{X}_2 + K_2 X_2^{3/2}). \quad (2)$$

For the chosen model setup, we consider the kinetic friction to be the same as the static friction. The adopted friction law for this illustrative example, resembles the Amontons-Coulomb's law [32,33], since the corresponding friction force is directly linked to a constant coefficient of friction, and proportional to the normal force. The direction of the friction force is established through a "signum" function assigned to the coefficient of friction, which reads as follows

$$\mu(V_r) = \mu_s \text{sgn}(V_r), \quad (3)$$

where $\mu_s$ is the static friction coefficient and $V_r$ is the relative velocity. Regarding the external load, both tangential and normal loading characterized by a frequency $\Omega_e$ and amplitude $M\alpha\Omega_e^2$ are applied as shown in Fig. 1. The equations of motion of the system then become

$$\begin{aligned} &\begin{bmatrix} 1 & 0 \\ 0 & 1 \end{bmatrix}\begin{pmatrix} \ddot{X}_1 \\ \ddot{X}_2 \end{pmatrix} + \begin{bmatrix} 2\beta_1\omega_1 & 0 \\ 0 & 2\beta_2^*\omega_2^* X_2^{3/2} \end{bmatrix}\begin{pmatrix} \dot{X}_1 \\ \dot{X}_2 \end{pmatrix} \\ &\quad + \begin{bmatrix} \omega_1^2 & 0 \\ 0 & \omega_2^{*2} \end{bmatrix}\begin{pmatrix} X_1 \\ X_2^{3/2} \end{pmatrix} \\ &\quad + \begin{pmatrix} \mu_s \text{sgn}(\dot{X}_1 - V_b)(2\beta_2^*\omega_2^* X_2^{3/2}\dot{X}_2 + \omega_2^{*2} X_2^{3/2}) \\ -g \end{pmatrix} \\ &= \begin{pmatrix} \alpha\Omega_e^2 \sin(\Omega_e t) \\ -\alpha\Omega_e^2 \sin(\Omega_e t) \end{pmatrix}, \end{aligned} \quad (4)$$

where $\beta_1 = \frac{C_1}{2M\omega_1}$, $\beta_2^* = \frac{C_2}{2M\omega_2^*}$, $\omega_1^2 = \frac{K_1}{M}$, $\omega_2^{*2} = \frac{K_2}{M}$ and $V_r$ is written in terms of $\dot{X}_1$ and $V_b$. Note that while $\beta_1$ is dimensionless, $\beta_2^*$ has the dimension of $\frac{1}{\text{m}^{5/4}}$ and instead of $\frac{\text{rad}}{\text{s}}$, $\omega_2^*$ has the dimension of $\frac{\text{rad}}{\text{m}^{1/4}\text{s}}$. Thus, the system described in Eq. (4) consists of two nonlinearly one-way coupled subsystems where the first subsystem is coupled to the second one through the friction force.

It is important to note that the tangential and normal excitation applied to the system have the same magnitude and frequency, with no phase shift between them. This type of loading can occur, for example, if an external force is applied at a 45-degree angle relative to the tangential direction of the mass. However, for the sake

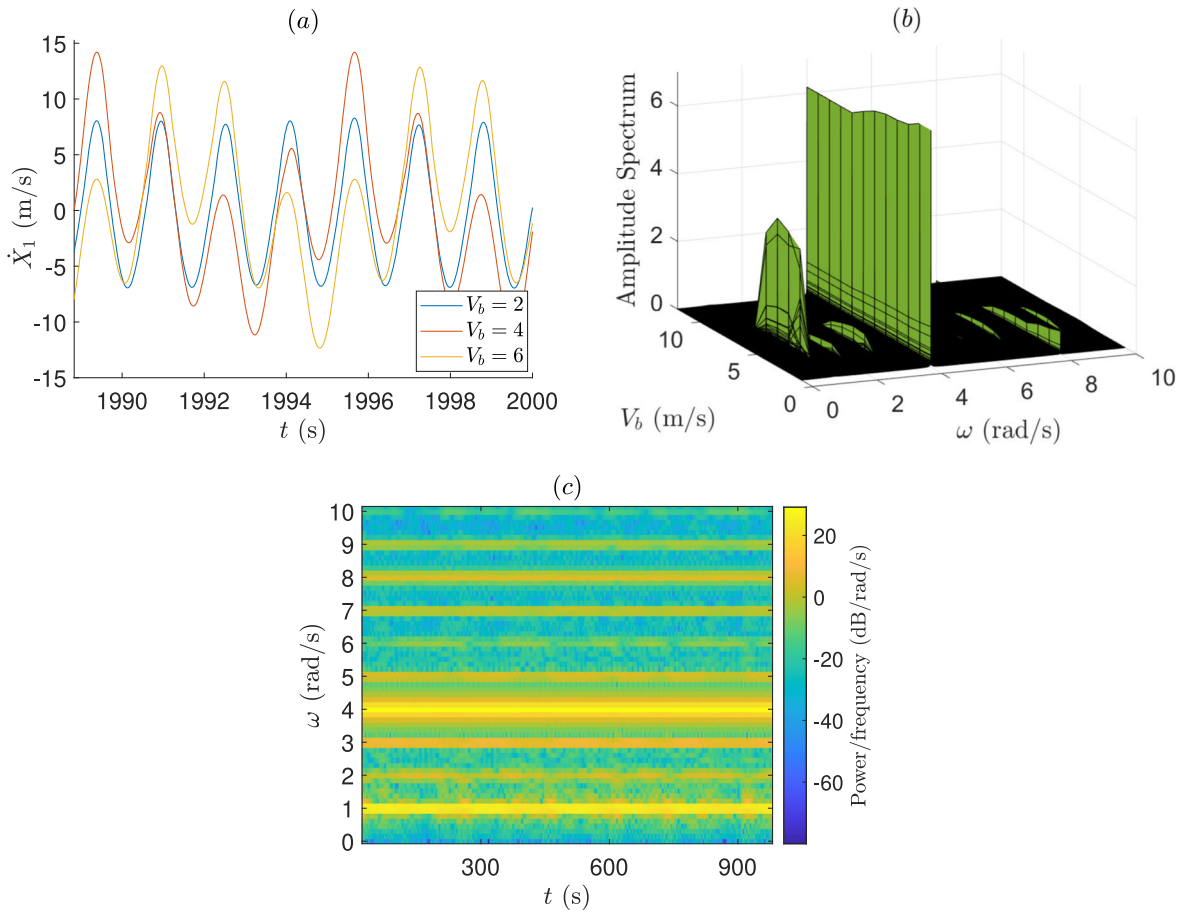


**Fig. 2** **a** Comparison of the velocity response in the tangential direction for different $V_b$ values; **b** Amplitude spectrum of the velocity $\dot{X}_1$; **c** Spectrogram visualising the variation of frequency spectrum with time for $V_b = 4$ m/s ($\omega_1 = 1\ \frac{\text{rad}}{\text{s}}$, $\omega_2^* = 0.5\ \frac{\text{rad}}{\text{m}^{1/4}\text{s}}$, $\beta_1 = 0.1$, $\beta_2^* = 0.15\frac{1}{\text{m}^{5/4}}$, $\alpha = 2$ m, $\Omega_e = 4\ \frac{\text{rad}}{\text{s}}$ and $\mu_s = 0.4$)

of analysis, an example with a phase shift of $\pi/2$, as well as an example with different excitation frequencies is examined in Sect. 3, to demonstrate that the investigated mechanism of friction-induced vibrations can still occur under these conditions.

## 3 Preliminary numerical analysis

To obtain the numerical solutions of the velocity response for different loading scenarios and system parameters, the equations of motion, Eq. (4), are solved numerically using the MATLAB solver ode45. To ensure that the chosen integration scheme appropriately captures the system's dynamics, for all the cases studied, the system's energy balance is verified, confirming that energy conservation is maintained. Figure 2a shows the numerical solution of the velocity response along the tangential direction for 3 different values of the belt velocity and for an external excitation driven at 4 rad/s. Note that the chosen time-window in Fig. 2a, is far away from the initial transient part of the response. As illustrated in Fig. 2a, different $V_b$ values lead to variations in the velocity response. Most importantly, oscillations of several periods are present in the dynamic response.

To get an overview of the spectral content, the Fast Fourier Transform (FFT) is applied over the entire time span, and the corresponding amplitude spectrum is displayed in Fig. 2b. The figure reveals a distinct peak not only at the excitation frequency, $\Omega_e = 4$ rad/s, but also at $\omega = 1$ rad/s. The latter corresponds to the natural frequency $\omega_1$ of the system along the tangential direction.

The peak is present for certain values of belt velocities and vanishes after $V_b \approx 8$ m/s. Thus, the response oscillates not only at the excitation frequency but also at the natural frequency $\omega_1$. Due to the non-linearity, other peaks are observed in the amplitude spectrum. As the nonlinearity is neither purely even nor purely odd, it leads to a mix of even and odd harmonics. However, they have small amplitudes and subsequently small significance on the response. In Fig. 2c, a spectrogram is depicted, visualising how the frequency spectrum varies with time. As indicated in the spectrogram, the peak at $\omega = 1$ rad/s persists throughout the whole duration and is not solely a result of the transient part of the response.

In the scenario depicted in Fig. 2, the excitation frequency $\Omega_e$ is an integer multiple of the natural frequency $\omega_1$. However, even with non-integer multipliers, the peak at $\omega_1$ is still present. For instance, as shown in Appendix A.1, when the excitation frequency is set to 4.5 rad/s, the peak at $\omega_1$ remains evident. Moreover, the peak at $\omega_1$ also occurs for cases when frequencies of excitation of the tangential and normal forcing are different from each other. As illustrated in Appendix A.1, when the excitation frequencies are 6 rad/s and 4 rad/s for the tangential and normal directions, respectively, the amplitude spectrum of the velocity response $\dot{X}_1$ still exhibits notable peaks at $\omega_1$ alongside the two excitation frequencies and other harmonics. Thus, the oscillations at the natural frequency $\omega_1$ indicate the presence of friction-induced vibrations. In the examples discussed so far, no phase shift has been observed between the tangential and normal loading. However, the friction-induced vibrations can still occur when a phase shift of $\pi/2$ is present, even though the velocity range for which these vibrations appear differs. An additional example illustrating this is provided in Appendix A.1.

To understand the mechanism by which friction can induce vibrations, the time-evolving friction force is investigated, with reference to the change of the corresponding relative sliding velocity. Figure 3a shows a time-series of the velocity response along the tangential direction, characterized predominately by the forcing frequency and by the natural frequency $\omega_1$. The steady-state part is represented by the blue region, from which corresponding friction force versus relative sliding velocity plots are investigated.

Figure 3b presents such a plot obtained over one full period $T_1$ ($=\frac{2\pi}{\omega_1}$). The plot starts at the point indicated by the blue arrow, with the color transitioning from dark blue to lighter blue as it progresses. The annotated red arrows show regions where the friction force increases while the relative velocity decreases in magnitude, or vice versa, indicating a negative slope in the friction force-velocity relationship. This negative slope corresponds to a negative damping effect along the tangential direction, which triggers the motion of the corresponding vibrational mode. Thus, parametric excitation of the dissipative term leads to the occurrence of negative damping, the net presence of which (from viscous damping and friction force) in the tangential direction (in parts of the oscillation cycles) explains the emergence of the additional peak at $\omega_1$, and is the mechanism causing friction-induced oscillations. The

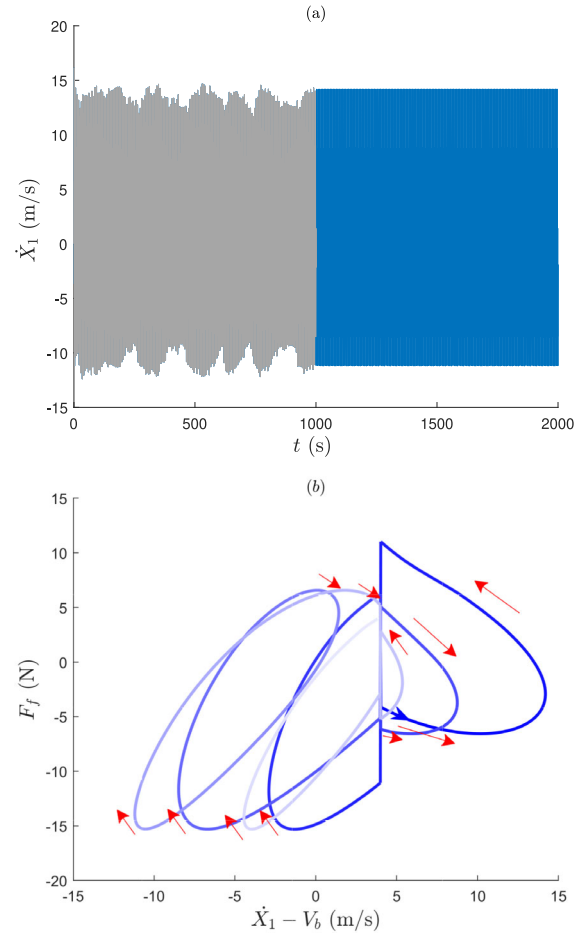


**Fig. 3** **a** Transient (grey) and steady-state (blue) part of the velocity response $\dot{X}_1$; **b** Friction force versus relative velocity. Belt velocity $V_b = 4$m/s. The rest of the parameters as in Fig. 2

presence of positive net damping in other parts of the oscillation cycles bounds the response.

To predict the onset of friction-induced vibrations, in the next section, a linearized stability analyses of the 2-DOF system is performed, considering both the harmonically unforced and forced scenarios (hereafter referred to simply as unforced and forced for brevity). For the forced cases, the linearized stability analysis is set up by taking advantage of the Method of Direct Separation of Motion.

## 4 Stability analysis of the steady sliding state

In this section, the stability analysis at the equalibrum point is carried out for both the unforced and forced system. To take into account the excitation-induced friction modulation effect, the Method of Direction Separation of Motion (MDSM) is used within the linearized stability framework. First, a linearized eigenvalue analysis is performed to assess the local stability of the steady sliding state of the system. Then, the Routh-Hurwitz stability criterion is applied to examine how various parameters influence the stability.

### 4.1 Jacobian linearization and stability analysis of the unforced system

The stability analysis of the unforced system is conducted by calculating the complex eigenvalues of the linearized system. To determine such eigenvalues, the Jacobian matrix is used. The initial stage in the Jacobian linearization process involves identifying the equilibrium points of the system. To accomplish this, the equations of motion are expressed in the following state-space form

$$Y_1 = \dot{X}_1 \tag{5}$$

$$\dot{Y}_1 = -2\beta_1\omega_1 Y_1 - \omega_1^2 X_1 + \mu_s(2\beta_2^*\omega_2^* X_2^{3/2} Y_2 + \omega_2^{*2} X_2^{3/2}) \tag{6}$$

$$Y_2 = \dot{X}_2 \tag{7}$$

$$\dot{Y}_2 = -2\beta_2^*\omega_2^* X_2^{3/2} Y_2 - \omega_2^{*2} X_2^{3/2} + g \tag{8}$$

equivalent to Eq. (4) for $\dot{X}_1 < V_b$ (the mass never overtakes the belt) and $X_2 > 0$ (non-jumping case). Setting the Eqs. (5)- (8) to zero, the equilibrium points are

$$(X_1^0, Y_1^0) = \left(\frac{\mu_s g}{\omega_1^2}, 0\right),$$

$$(X_2^0, Y_2^0) = \left(\left(\frac{g}{\omega_2^{*2}}\right)^{2/3}, 0\right). \tag{9}$$

By taking the partial derivatives of equations (5)-(8), the Jacobian matrix is obtained

$$\mathbf{J} = \begin{bmatrix} \frac{\partial \dot{X}_1}{\partial X_1} & \frac{\partial \dot{X}_1}{\partial Y_1} & \frac{\partial \dot{X}_1}{\partial X_2} & \frac{\partial \dot{X}_1}{\partial Y_2} \\ \frac{\partial \dot{Y}_1}{\partial X_1} & \frac{\partial \dot{Y}_1}{\partial Y_1} & \frac{\partial \dot{Y}_1}{\partial X_2} & \frac{\partial \dot{Y}_1}{\partial Y_2} \\ \frac{\partial \dot{X}_2}{\partial X_1} & \frac{\partial \dot{X}_2}{\partial Y_1} & \frac{\partial \dot{X}_2}{\partial X_2} & \frac{\partial \dot{X}_2}{\partial Y_2} \\ \frac{\partial \dot{Y}_2}{\partial X_1} & \frac{\partial \dot{Y}_2}{\partial Y_1} & \frac{\partial \dot{Y}_2}{\partial X_2} & \frac{\partial \dot{Y}_2}{\partial Y_2} \end{bmatrix} = \begin{bmatrix} 0 & 1 & 0 & 0 \\ -\omega_1^2 & -2\beta_1\omega_1 & \mu_s(3\beta_2^*\omega_2^* X_2^{1/2} Y_2 + \frac{3}{2}\omega_2^{*2} X_2^{1/2}) & 2\mu_s\beta_2^*\omega_2^* X_2^{3/2} \\ 0 & 0 & 0 & 1 \\ 0 & 0 & -3\beta_2^*\omega_2^* X_2^{1/2} Y_2 - \frac{3}{2}\omega_2^{*2} X_2^{1/2} & -2\beta_2^*\omega_2^* X_2^{3/2} \end{bmatrix}, \tag{10}$$

and evaluating the Jacobian at the equilibrium points, the linearization reads as follows

$$\mathbf{J}^0 = \begin{bmatrix} 0 & 1 & 0 & 0 \\ -\omega_1^2 & -2\beta_1\omega_1 & \frac{3}{2}\mu_s\omega_2^{*2}\left(\frac{g}{\omega_2^{*2}}\right)^{1/3} & \frac{2\mu_s\beta_2^* g}{\omega_2^*} \\ 0 & 0 & 0 & 1 \\ 0 & 0 & \frac{-3}{2}\omega_2^{*2}\left(\frac{g}{\omega_2^{*2}}\right)^{1/3} & \frac{-2\beta_2^* g}{\omega_2^*} \end{bmatrix}. \tag{11}$$

The complex eigenvalues, $\lambda$, are found by solving the determinant

$$|\lambda\mathbf{I} - \mathbf{J}^0| = 0. \tag{12}$$

The roots of the characteristic equation are computed numerically, and in Fig. 4, the real part $\sigma$, indicating the growth rate, and the imaginary part $\omega$, representing the oscillation frequencies of the complex eigenvalues $\lambda$ are depicted. These are plotted for a range of $\beta_1$ values, while maintaining all other parameters constant as in Fig. 2. The stability of the linearized and unforced system is determined by the sign of $\sigma$. If the sign of the sigma of all roots is negative, the unforced system is stable.

For $\beta_1 \geq 1$, four negative real $\sigma$ values are present in Fig. 4a and the oscillation frequencies $\omega$ of the modes

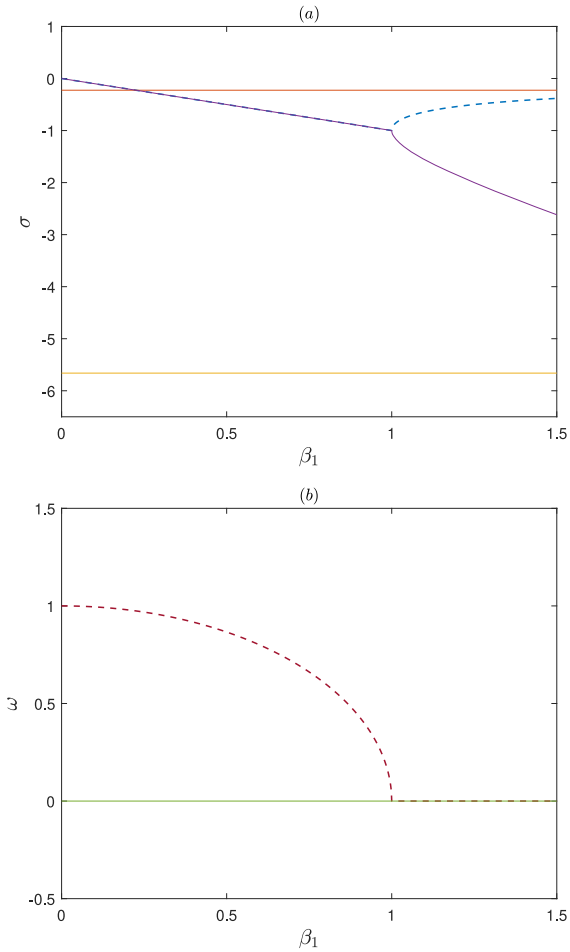


**Fig. 4** **a** Real part $\sigma$ versus $\beta_1$; **b** Imaginary part $\omega$ versus $\beta_1$. $\Omega_e$ =0 (unforced system) and the rest of parameters as in Fig. 2

merge and equal zero, as shown in Fig. 4b, leading to an overdamped system. For $\beta_1 < 1$, only one mode experiences overdamping. Still, all the $\sigma$ values are negative, meaning that the unforced linearized system is stable. It is worth highlighting that the adopted system is different from the 2-DOF models considered in [5–7] where a mode-coupling mechanism due to the presence of a diagonal spring enabled the instability to occur in the corresponding unforced systems, and the effect of systems parameters such as damping, contact nonlinearity or friction coefficient on the instability were studied. It should also be noted that even though the friction coefficient $\mu_s$ appears in the Jacobian matrix $\mathbf{J}^0$, Eq. (11), it does not appear in the characteristic equation derived from Eq. (12). Consequently, contrary to systems with the mode-coupling mechanism enabled by a diagonal spring [5], the stability of the unforced system is not influenced by the friction coefficient. In the following section, the stability analysis of the linearized forced system is investigated.

### 4.2 Jacobian linearization and stability analysis of the forced system

Here, the 2-DOF system in the presence of tangential and normal harmonic excitation is considered, and the effect of excitation on the stability of the steady sliding state is investigated. To examine this, the Method of Direct Separation of Motion is used which separates the "slow" and "fast" components of the motions [18,27,28]. The slow motions, the stability of which is investigated, are those of primary interest, whereas the excitation is accounted for only by its "average" influence. The separation of motions $X_1(\tau)$ and $X_2(\tau)$ into the slow and fast components reads as follows

$$X_1(\tau) = Z_1(\tau) + \Omega^{-1}\Phi_1(\tau, \Omega\tau) \tag{13}$$

$$X_2(\tau) = Z_2(\tau) + \Omega^{-1}\Phi_2(\tau, \Omega\tau), \tag{14}$$

where $Z_1(\tau)$, $Z_2(\tau)$ describe the slow motions and $\Phi_1$, $\Phi_2$ describe the fast motions at the rate of the external excitation. To make the transformation of variables from $\mathbf{X}$ to $\mathbf{Z}$ and $\Phi$ unique, the following constraint is applied

$$\langle \Phi(\tau, \Omega\tau) \rangle = \frac{1}{2\pi} \int_0^{2\pi} \Phi(\tau, \Omega\tau) \mathrm{d}(\Omega\tau) = 0, \tag{15}$$

where $<>$ defines the average operator over the period of the rapidly oscillating component.

The application of the MDSM into the equations of motion is greatly complicated by the form of the nonlinearity $X_2^{3/2}$. Therefore, before substituting Eq. (13) and Eq. (14) into Eq. (4), to make the solution process more tractable, the nonlinearity is expressed in the form of a polynomial. Performing a third-order least-squares fit to the nonlinearity over the interval $0 < X_2 < X_{2,\max}$ yields to

$$X_2^{3/2} = c_3 X_2^3 + c_2 X_2^2 + c_1 X_2 + c_0, \tag{16}$$

where

$$c_3 = -\frac{8}{33 X_{2,\max}^{3/2}}, c_2 = \frac{72}{77 X_{2,\max}^{1/2}},$$

$$c_1 = \frac{24 X_{2,\max}^{1/2}}{77}, c_0 = -\frac{8 X_{2,\max}^{3/2}}{1155}, \tag{17}$$

and $X_{2,\max}$ is the maximum value of $X_2$ encountered. The series approximation has a maximum error of about $10^{-2}$. Similar fits for the nonlinearity $X_2^{3/2}$ have been used by Bryant [34] and Hess and Soom [35]. Substituting Eq. (16) into Eq. (4), separating the motions $[\mathbf{X}] = [X_1\ X_2]^{\mathrm{T}}$ into the components $[\mathbf{Z}] = [Z_1\ Z_2]^{\mathrm{T}}$ and $[\Phi] = [\Phi_1\ \Phi_2]^{\mathrm{T}}$ and making use of the averaging operation, the equations of motion for the components in $\mathbf{Z}$ are obtained

$$\ddot{Z}_1 + 2\beta_1\omega_1\dot{Z}_1 + \omega_1^2 Z_1 + \bar{\mu}(2\beta_2^*\omega_2^*\dot{Z}_2 + \omega_2^{*2}) \times(c_3 Z_2^3 + c_2 Z_2^2 + c_1 Z_2 + c_0) = 0 \tag{18}$$

$$\ddot{Z}_2 + (2\beta_2^*\omega_2^*\dot{Z}_2 + \omega_2^{*2}) \times(c_3 Z_2^3 + c_2 Z_2^2 + c_1 Z_2 + c_0) - g = 0, \tag{19}$$

where $\bar{\mu}(V_r)$ is the effective friction characteristic (still to be defined). The equations of motion for the components in $\Phi$ are shown in Appendix A.3. Equations (18) and (19) for the slow motions are similar in form to Eq. (4) for the total motion, but with the excitation accounted for by the effective friction $\bar{\mu}$ instead of the ordinary $\mu$ and the nonlinearity expressed in the form of the polynomial given by Eq. (16). The utilization of the polynomial form was needed to simplify the application of the MDSM. Conversely, when applying the Jacobian linearization to the equations of slow motion, Eqs. (18) and (19), the polynomial form of the nonlinearity makes the determination of the equilibrium points cumbersome. Hence, it proves more convenient to handle the nonlinearity expressed as $Z_2^{3/2}$. Thus, Eqs. (18) and (19) are rewritten as

$$\ddot{Z}_1 + 2\beta_1\omega_1\dot{Z}_1 + \omega_1^2 Z_1 + \bar{\mu}(2\beta_2^*\omega_2^*\dot{Z}_2 + \omega_2^{*2})Z_2^{3/2} = 0 \tag{20}$$

$$\ddot{Z}_2 + (2\beta_2^*\omega_2^*\dot{Z}_2 + \omega_2^{*2})Z_2^{3/2} - g = 0. \tag{21}$$

To determine the Jacobian matrix, Eq. (20) and Eq. (21) are written in the state-space form and the equilibrum points are found setting the latter to zero, see Appendix A.2. The Jacobian evaluated at the equilibrium points is

$$\mathbf{J}_f^0 = \begin{bmatrix} 0 & 1 & 0 & 0 \\ -\omega_1^2 & -2\beta_1\omega_1 + \bar{\mu}' g & \frac{3}{2}\bar{\mu}^0\omega_2^{*2}\left(\frac{g}{\omega_2^{*2}}\right)^{1/3} & \frac{2\bar{\mu}^0\beta_2^* g}{\omega_2^*} \\ 0 & 0 & 0 & 1 \\ 0 & 0 & \frac{-3}{2}\omega_2^{*2}\left(\frac{g}{\omega_2^{*2}}\right)^{1/3} & \frac{-2\beta_2^* g}{\omega_2^*} \end{bmatrix}, \tag{22}$$

where the index $f$ refers to the forced system and $\bar{\mu}'$ denotes the slope of the effective friction at the equilibrium point; note that the linearization of the effective friction expression is necessary for the formulation of the Jacobian of the system. To find the expression of the effective friction $\bar{\mu}$ in the sliding regime, in a previous study where linear contact properties were used [18], it was demonstrated that the velocity response function of the system can be exploited. For that system, the effective friction expression is

$$\bar{\mu}(V_r) = \begin{cases} \mu_s\left(1 - \frac{2}{\pi}\arccos\left(\frac{\dot{Z}_1 - V_b}{\hat{V}}\right)\right) & \text{for } |\dot{Z}_1 - V_b| \le \hat{V} \\ \mu_s \mathrm{sgn}(\dot{Z}_1 - V_b) & \text{for } |\dot{Z}_1 - V_b| \ge \hat{V} \end{cases}, \tag{23}$$

where $\hat{V}$ corresponds to the amplitude of the velocity response obtained for linear contact properties. Then, $\bar{\mu}'$ and $\bar{\mu}^0$ are obtained through the linearization process as follows

$$\bar{\mu} = \bar{\mu}^0 + \left.\frac{\partial\bar{\mu}}{\partial\dot{Z}_1}\right|_{\dot{Z}_1=0}\dot{Z}_1 + O(\dot{Z}_1)^2, \tag{24}$$

where

$$\bar{\mu}^0 = \bar{\mu}(\dot{Z}_1^0), \quad \bar{\mu}' = \frac{2\mu_s}{\pi\hat{V}\sqrt{1 - (V_b/\hat{V})^2}} \tag{25}$$

for $\hat{V} > V_b$.

The complex eigenvalues, $\lambda_f$ are found from the determinant

$$|\lambda_f\mathbf{I} - \mathbf{J}_f^0| = 0, \tag{26}$$

which is solved numerically, and the real part, $\sigma$, of the complex eigenvalues, $\lambda_f$, is plotted in Fig. 5a for a range of $V_b$ values and the same parameters used as in Fig. 4. While in Fig. 4a, the $\sigma$ values are all negative, Fig. 5a depicts positive $\sigma$ values for $V_b$ belt velocities smaller than approximately 8 m/s. The positive $\sigma$ values indicate instability for the corresponding range of $V_b$ values. This range of belt velocities correlates to the one for which the spectral response peak at $\omega_1$ is shown in the amplitude spectrum in Fig. 2b. Thus, $V_b \approx 8$ m/s, is the bifurcation point below which friction-induced vibrations are observed. For $V_b$ values higher than 8 m/s, a sudden drop to negative $\sigma$ values is depicted. In this range of $V_b$ values, the amplitude of the velocity response $\hat{V}$ is smaller than the belt velocity, indicating that the effective friction is constant and its slope is zero. Consequently, the excitation has no impact on stability, the characteristic equation of the

forced system matches that of the unforced system, and the system is stable at the equilibrium point.

Small discrepancies in the value of the bifurcation point predicted by the stability analysis and that observed in the numerical results are due to approximations in the stability analysis. As mentioned above, the expression for effective friction is derived for a system with linear contact properties (which does not experience friction-induced oscillations). However, as will be shown in Sect. 4, since the stability analysis depends on the slope of the effective friction curve, the expression obtained for linear contact properties remains a good approximation. If for a specific parameter space, the slope of the effective friction in the current systems significantly differs from the slope in the system with linear contact properties, the discrepancy in the results obtained through stability and numerical analysis will increase. In the next section, the effect of the slope of effective friction curve on the stability will be discussed in more detail.

The findings outlined here complement and further extend the domain of investigation explored in Thomsen [13] and Hoffmann [14], in which external excitation was employed to quench the initially unstable system at the equilibrium point. In the current investigated model, the unforced system is stable and the presence of an harmonic excitation may induce instability of the steady sliding state. The current study also extends the results obtained by Michaux and coworkers [15], since their research indicates that an excitation can stabilise or destabilize a single degree of freedom system governed by a decreasing friction law, while in this study, instability is observed despite considering the Amontons-Coulomb law. Moreover, it should be noted that the stability analysis presented in this study does not provide insights into the stick–slip behavior of the investigated system. Although a negative $\sigma$ value indicates system stability, it does not offer information on whether the system may exhibit stick–slip or not.

It is important to highlight that even though a value of $\beta_2^* = 0.15$ is utilized, the system is overdamped along the vertical direction due to the presence of the nonlinearity. This holds true for both unforced and forced scenarios, as depicted in Figs. 4b and 5b. In the case where linear contact properties are considered, as discussed in [18], a $\beta_2$ value greater than 1 would lead to overdamping. For instance, if $\beta_2 = 3$, the system with linear contact properties is overdamped in the $X_2$ direction and locally unstable along the $X_1$ direction, leading

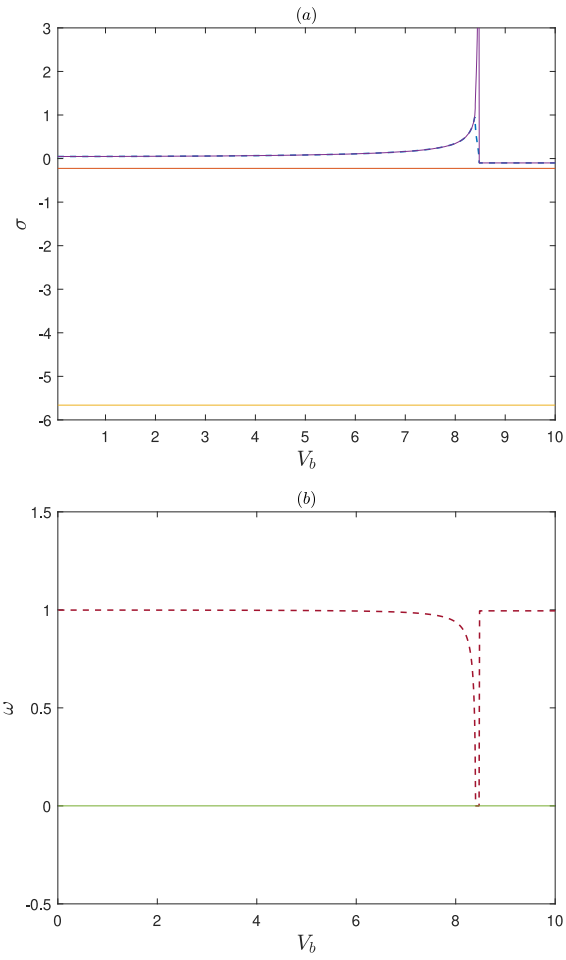


**Fig. 5** **a** Real part $\sigma$ versus $V_b$; **b** Imaginary part $\omega$ versus $V_b$. $\Omega_e = 4$ rad/s (forced system) and the rest of parameters as in Fig. 2

to friction-induced vibrations for belt velocities lower than the bifurcation belt velocity (see Appendix A.3 for further details). Hence, friction-induced oscillations can occur in an overdamped system with linear contact properties as well. It should be noted that while the effect of damping on friction-induced vibrations is discussed here, systems with both linear and nonlinear contact properties can also experience friction-induced vibrations when they are underdamped by altering the other parameter values. This is shown in the next section, where the Routh-Hurwitz criterion is used to study the effect of the model parameters on the evolution of the bifurcation point of the system.

### 4.3 Routh-Hurwitz stability criterion

In the previous section, the stability of the steady siding state was determined using the roots of the characteristic equation. Here, the Routh-Hurwitz stability criterion is used as it provides the means for testing the stability without having to obtain the roots of the characteristic equation. Moreover, utilizing this approach enables the derivation of analytical expressions of the Routh-Hurwitz coefficients (in relation to system parameters) that can be employed to determine which parameters govern the stability and how they effect the evolution of the bifurcation point of the system. Considering Eq. (26), the 4-th order characteristic polynomial can be written as

$$\lambda^4 + a_1\lambda^3 + a_2\lambda^2 + a_3\lambda + a_4 = 0. \tag{27}$$

for which the expressions of $a_1, a_2, a_3$ and $a_4$ are shown in Appendix A.4. Moreover, applying the Routh-Hurwitz criterion to this characteristic equation gives the four following coefficients

$$\begin{aligned} H_1 &= a_1 \\ H_2 &= a_1a_2 - a_3 \\ H_3 &= a_1a_2a_3 - a_3^2 - a_4a_1^2 \\ H_4 &= a_1a_2a_3a_4 - a_1a_4^2 - a_4a_3^2. \end{aligned} \tag{28}$$

If all these coefficients are positive, the steady sliding state is stable. When at least one of the coefficients is negative, the steady sliding state is unstable

Figure 6a portrays the effect of $V_b$ and $\beta_1$. Since for the parameters chosen, $H_3$ governs the stability, only the contour line of $H_3$ is shown. The shaded area corresponds to negative values of $H_3$ and, as a result, represents the region in which friction-induced vibration can occur (in the graphs's legend, it is indicated as "unstable"). It can be seen that as the values of the damping coefficient $\beta_1$ increase, the range of belt velocities $V_b$ for which the steady sliding state is unstable decreases. Thus, a higher $\beta_1$ value helps in decreasing the range of belt velocities where friction-induced vibrations can occur. This can be explained by the net damping along the tangential direction turning positive once the dissipated energy due to viscosity and due to the friction force exceeds the energy associated with the negative damping effect of the friction force. Considering the approximations introduced for the linearized stability analysis, a numerical validation study of the effect of $\beta_1$ on the system stability is presented in Fig. 17 in Appendix A.5, demonstrating a good qualitative and quantitative agreement between the numerical results and the stability diagram. A comprehensive discussion can be found in Appendix A.5.

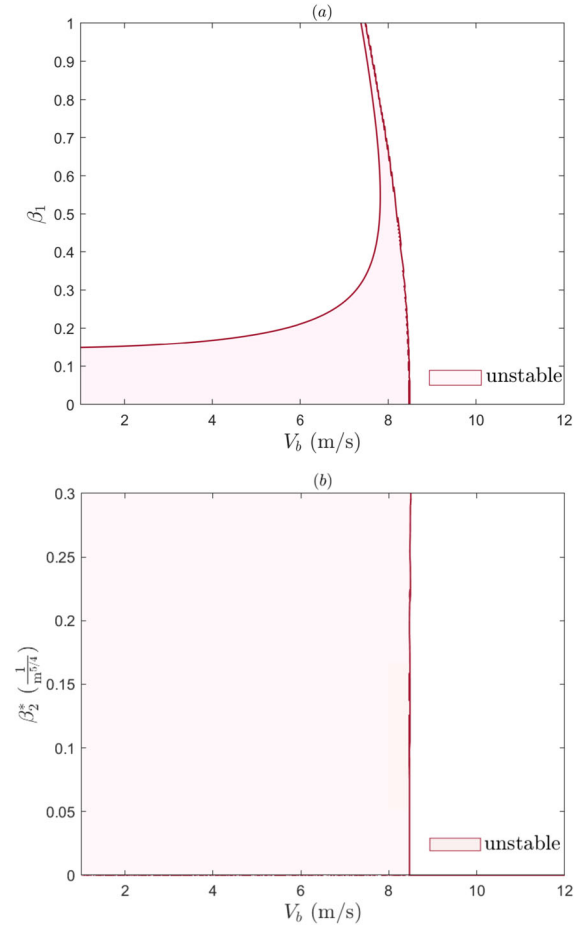


**Fig. 6** Parametric study on the stability of the system: **a** effect of damping ratio $\beta_1$; **b** effect of damping ratio $\beta_2^*$

The effect of damping ratio in the normal direction $\beta_2^*$ is shown in Fig. 6b where the contour line of $H_3$ is plotted with the shaded area corresponding to the unstable region. This region remains relatively the same for increased $\beta_2^*$ values (limited to $\beta_2^* = 0.3$ because the system is overdamped even for the value of 0.15 used in this study.) Thus, unlike $\beta_1$, variations in $\beta_2^*$ have little effect on the unstable region. The numerical validation plots in Fig. 18 show a good qualitative agreement. While the quantitative match is good within the stability region, discrepancies are observed in the unstable region for certain parameter values (see Appendix A.5).

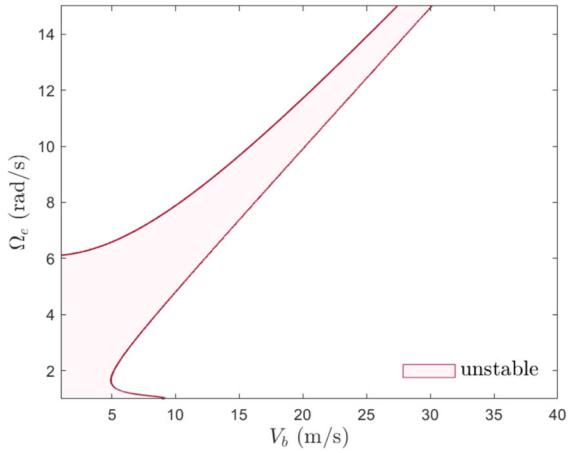


**Fig. 7** Parametric study on the stability of the system: effect of excitation frequency $\Omega_e$. The rest of the parameters as in Fig. 2

To assess the influence of the excitation frequency $\Omega_e$, Fig. 7 shows the contour line of $H_3$ as a function of $\Omega_e$ and $V_b$. The unstable region decreases for increased $\Omega_e$ values. Thus, a higher $\Omega_e$ value helps in decreasing the range of belt velocities where friction-induced vibrations occur. As mentioned previously, it is important to note that the unstable region gives no information about the stick–slip behaviour. For the excitation frequency value used in this study, i.e. $\Omega_e = 4$ rad/s, Fig. 7 shows that for belt velocities smaller than the bifurcation point of $V_b \approx 8$ m/s, friction-induced oscillations occur and the numerical results, Fig. 2, indicate that the system is in the sliding state. For different excitation frequencies, however, the system might exhibit a stick–slip behaviour. For example, for excitation frequencies $\Omega_e = 8$ rad/s and $\Omega_e = 10$ rad/s, the numerical validation plots presented in Fig. 19 in Appendix A.5 show that stick–slip behavior occurs within the stable regions depicted in the stability diagram (for $V_b$ values less than 10 m/s and 15 m/s, respectively). These results contradict those by previous studies [13–15] where high excitation frequencies were used to quench stick–slip motion. The numerical results also indicate that the stability diagram underestimates the size of the unstable region as excitation frequencies increase.

In Fig. 8a, b the influence of the stiffness, by varying the values of $\omega_1$ and $\omega_2^*$ values. As the $\omega_1$ value increases, the unstable region decreases, reaching its minimum when $\omega_1 = \Omega_e = 4$ rad/s. However, as $\omega_1$ continues to increase beyond this point, the unstable region begins to expand. The numerical validation plots shown in Fig. 20 in Appendix A.5 display a good qualitative and quantitative match. Regarding $\omega_2^*$, the numerical results show stick–slip regions for increasing $\omega_2^*$ values (the actual frequency being the square root of the linearised stiffness term, i.e., $\frac{3}{2}\omega_2^{*2}\left(\frac{g}{\omega_2^{*2}}\right)^{1/3}$). Therefore, the y-axis of the stability diagram is limited to $\omega_2^* = 2\ \frac{\text{rad}}{\text{m}^{1/4}\text{s}}$. In Fig. 8b, it is shown that the unstable region slightly decreases by varying $\omega_2^*$. In Fig. 21, a good qualitative and quantitative agreement is shown with the numerical validation plots (Appendix A.5).

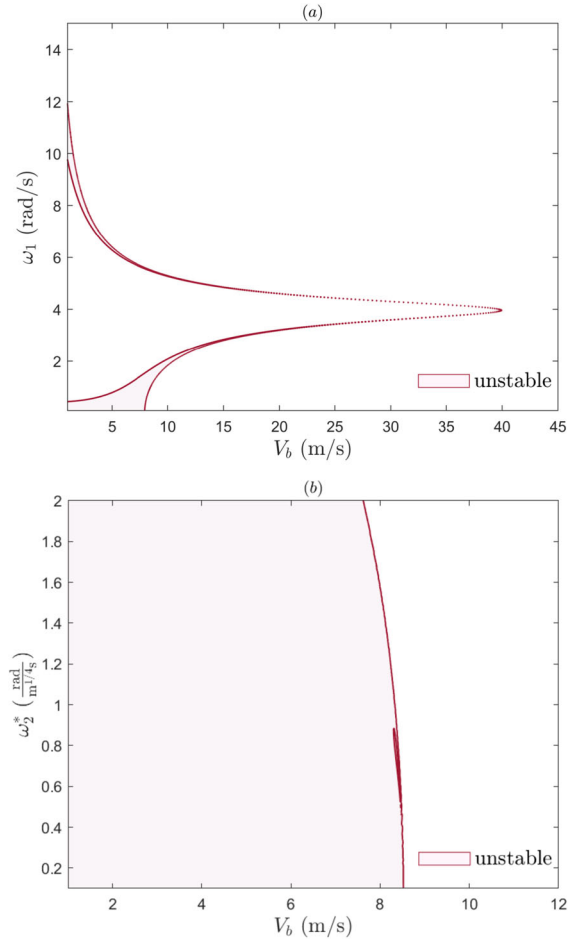


**Fig. 8** Parametric study on the stability of the system: **a** effect of $\omega_1$; **b** effect of $\omega_2^*$. The rest of the parameters are chosen as in Fig. 2

Lastly, the influence of $\bar{\mu}'$ is studied. While in the Jacobian matrix of the forced system in Eq. (22), both $\bar{\mu}'$ and $\bar{\mu}^0$ are present, in the expressions of $a_1$, $a_2$, $a_3$

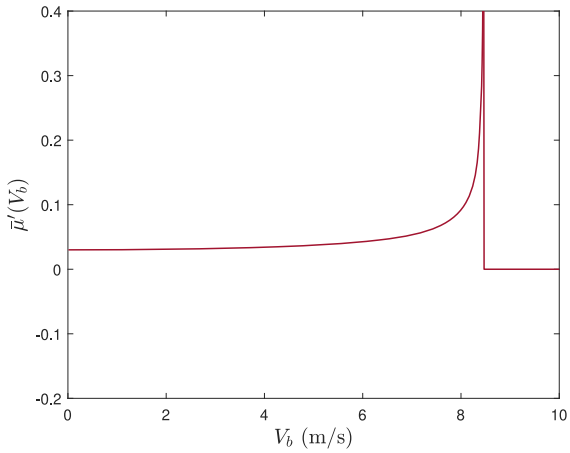


**Fig. 9** Slope of average friction versus belt velocity. Parameters as in Fig. 2

and $a_4$ of the characteristic equation, Eq. (27), only $\bar{\mu}'$ remains, meaning that the complex eigenvalues and also the Routh-Hurwitz coefficients, Eq. (28), depend only on $\bar{\mu}'$. Thus, the stability is influenced by the slope of the effective friction expression. As shown in Eq. (23), the effective friction expression is defined by a piece-wise function. For relative velocities smaller than $\hat{V}$, the average friction takes the shape of an arccosine, the slope of which increases with increasing $V_b$ value and goes to infinity as $V_b$ approaches the $\hat{V}$ value. For relative velocities bigger than $\hat{V}$, the average friction becomes the constant $\mu_s$ and its slope is zero. This behaviour is also portrayed in Fig. 9. When the slope $\bar{\mu}'$ becomes zero, the characteristic equation of the forced system aligns with that of the unforced system, indicating that the excitation has no influence on the stability. Thus, for $V_b$ exceeding $\hat{V}$, the system is stable, akin to the unforced system. For $V_b$ less than $\hat{V}$, slope values span from nearly zero to positive infinity (based on the parameters determining $\bar{\mu}'$). Hence, the stability is primarily governed by the system parameters such as damping, stiffness and frequency of excitation, as $\bar{\mu}'$ depends on these parameters.

## 5 Effect on friction modulation

In this section, the aim is to study the effect of friction-induced vibrations on friction modulation. In our previous work [18], it was demonstrated that effective friction expression is calculated using a cycle of the velocity response of the system in the steady-state regime.

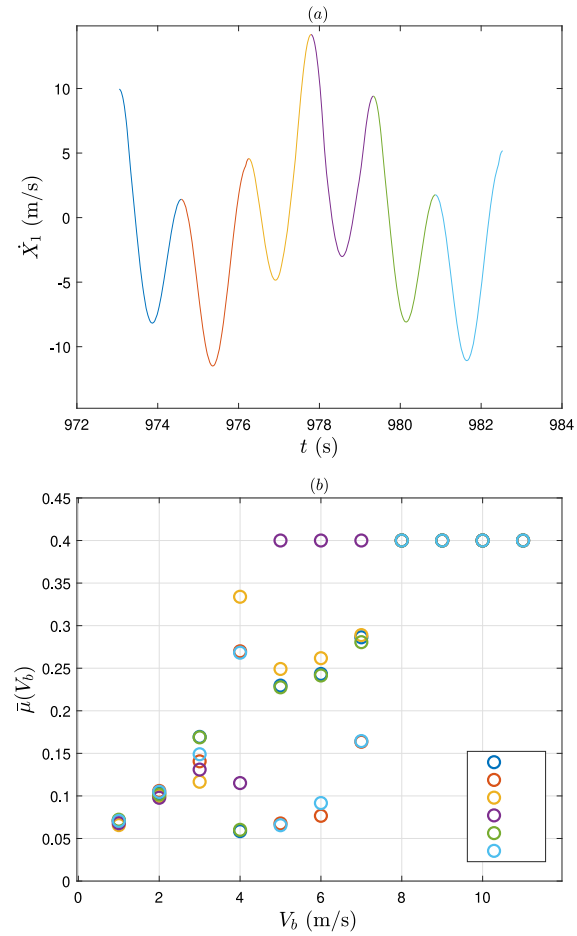


**Fig. 10** **a** Velocity response for $V_b = 4$ m/s; **b** Friction modulation obtained averaging over $\frac{2\pi}{\Omega_e}$. The cycle colors in plot **a** correspond to the colored circles in plot (**b**). Parameters as in Fig. 2

The direction of the friction force changes depending on the direction of relative velocity, and the effective friction is calculated by performing an averaging operation on the friction force over one cycle of oscillation. In case of no friction-induced oscillations, the variation in the cycles of the velocity response (due to higher harmonics) is negligible. For the system considered in this study, however, since oscillations at the natural frequency are also present, the calculation of the friction modulation is not that straightforward. Looking at the graph illustrating the numerically obtained velocity response for $\Omega_e = 4$ rad/s and $V_b = 4$ m/s, see Fig. 10a, the cycles differ from each other, since multiple oscillation periods are present. Consequently, the averaged friction values (averaging over $\frac{2\pi}{\Omega_e}$) derived

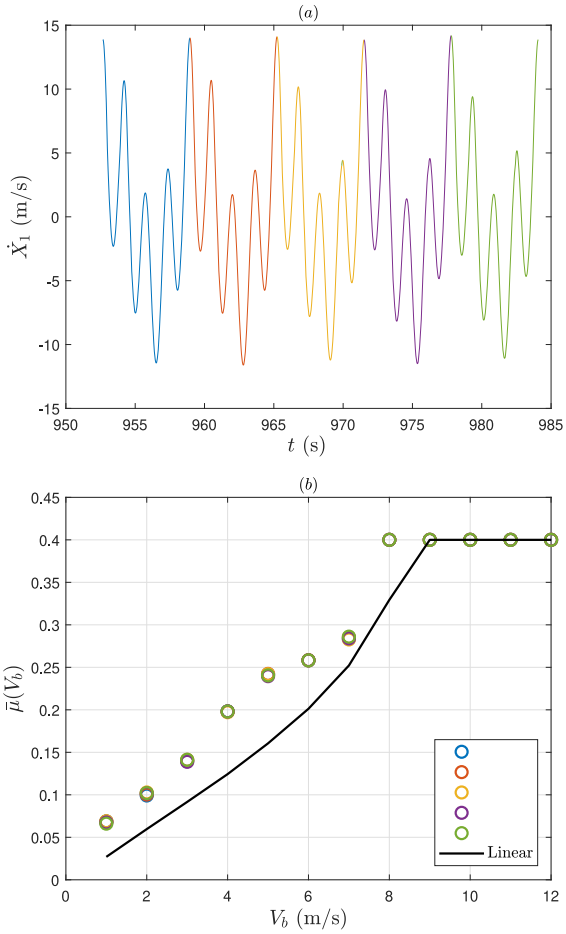


**Fig. 11** **a** Velocity response for $V_b = 4$ m/s; **b** Friction modulation obtained averaging over $\frac{2\pi}{\omega_1}$. The cycle colors in plot **a** correspond to the colored circles in plot (**b**). Parameters as in Fig. 2

from different cycles are not the same, as shown in Fig. 10b. The colors of the circles, which illustrate the effective friction values, align with the colors of the cycles employed in computing these effective friction values. As shown in Fig. 10b, there is a scatteredness in the effective friction values for belt velocities less than 8 m/s, corresponding to the bifurcation point (see Fig. 5). As a result of this scatteredness, there exist multiple effective friction values for a specific belt velocity.

If instead of using cycles aligning with the period of excitation frequency, as depicted in Fig. 10a, the averaging process is performed over $\frac{2\pi}{\omega_1}$ (associated with the first spectral peak in the amplitude spectrum shown in Fig. 2b), as illustrated in Fig. 11a, the outcomes presented in Fig. 11b are obtained, exhibiting a more repeatable trend for the effective friction values at different belt velocities. Additionally, the average friction plot derived using the stable system with linear contact properties (as done in [18]) is depicted by the black line, revealing lower average friction values (for $V_b < 9$ m/s) at a given belt velocity. It is worth mentioning that in this scenario, the excitation frequency is four times the natural frequency. Consequently, in the steady state, after four cycles corresponding to the excitation frequency period (Fig. 10a), the response repeats itself (Fig. 11a). Hence, opting for a different time window of at least four cycles and conducting averaging over $\frac{2\pi}{\Omega_e}$, as in Fig. 10b, or over $\frac{2\pi}{\omega_1}$, depicted in Fig. 11b, would yield the same outcomes.

Increasing the excitation frequency to $\Omega_e = 6$ rad/s, the results depicted in Fig. 12a are obtained, showing a bigger scatteredness in the effective friction values (the numerical validation plot is shown in Fig. 19a in Appendix A.5). Averaging over $\frac{2\pi}{\omega_1}$ instead, results again in almost no scatteredness, as shown in Fig. 12b. Compared to the stable linear case (see black continuous line in Fig. 12b), the effective friction values are higher for $V_b < 7$ m/s, lower for 8 m/s $< V_b <$ 15 m/s and equal to the linear case for $V_b > 16$ m/s. Thus, increasing the excitation frequency leads to an increase in scatteredness in Fig. 12a and in a variation of the effective friction values that, depending on the belt velocities, might either increase or decrease compared to the ones obtained for the stable system with linear contact properties, Fig. 12b.

In several theoretical and experimental works conducted on the effect of vibration-induced friction reduction, the measurements did not match the model predictions obtained assuming an Amontons-Coulomb law to model the friction force. Gutowski and Leus [36,37], for example, analysed the influence on the averaged friction force of an external forcing applied parallel and perpendicular to the sliding direction, respectively. While for the case of longitudinal excitation, the discrepancy of experimental measurements with the theoretical results obtained assuming Amontons-Coulomb friction law was not significantly large, for the case of transverse excitation significant mismatches were observed. To better catch the experimental behaviour, they used the Dahl and the Dupont models [23] that take into account a tangential contact stiffness. The Dahl friction model with different stiffness values was employed by Wang and coworkers as well and a qualitatively good match was obtained with the experi-

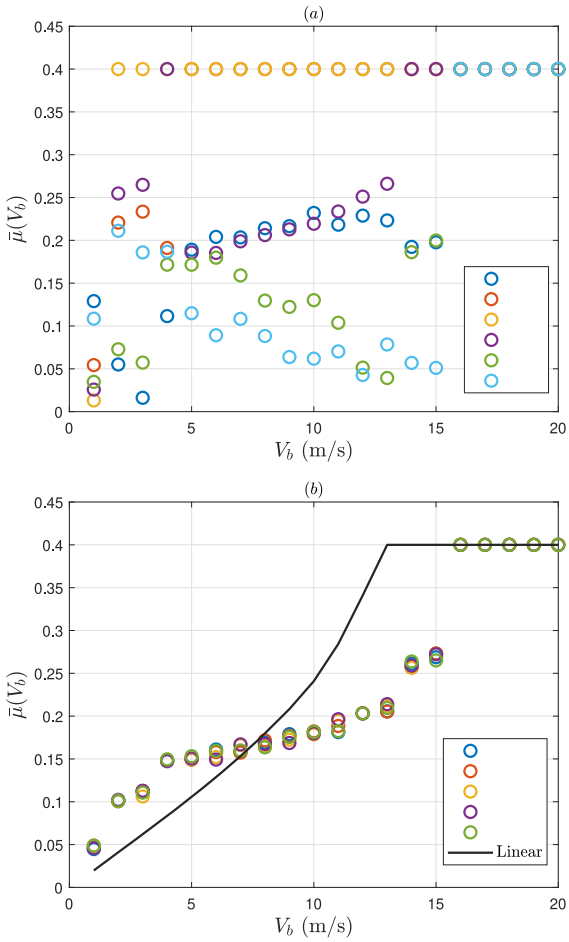


**Fig. 12** **a** Friction modulation obtained averaging over $\frac{2\pi}{\Omega_e}$; **b** Friction modulation obtained averaging over $\frac{2\pi}{\omega_1}$. The cycle colors in plot **a** correspond to the colored circles in plot (**b**). $\Omega_e = 6$ rad/s and the rest of the parameters as in Fig. 2

mental results [38,39]. Deviations were still observed for specific material combinations. Kapelke also used the Dupont model and the Amontons-Coulomb law to compare the experimental results to theoretical ones [22]. An excellent match between the experimental results and the elasto-plastic Dupont model was observed. However, to accurately catch the behaviour of the friction force reduction observed for tests carried out with high excitation frequencies, significantly different values of stiffness were needed for the Dupont model compared to the ones used for the low-frequency tests. Figure 13 shows the effective friction plots obtained using the Amontons-Coulomb law and both the full and reduced elasto-plastic model as conducted in [22]. The figure indicates that the elasto-

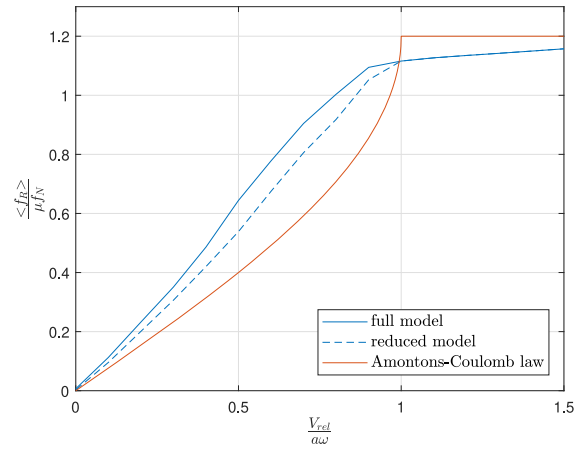


**Fig. 13** Friction-velocity characteristics: Amontons-Coulomb, reduced and full elasto-plastic friction model as in [22]

plastic friction model yields higher effective friction values than the Amontons-Coulomb law, similar to the results shown in Fig. 11b. Increasing the excitation frequency results in a different trend, Fig. 12b.

To summarise, in this study, the friction force is assumed to be proportional to the coefficient of friction and the normal force being time-varying and nonlinear. In other words, rather than considering a single degree of freedom system coupled to a Dahl and/or Dupont model (which includes a tangential contact stiffness), nonlinear contact properties along the normal direction are incorporated, which, if excited, generate a nonlinear time varying friction force. Hence, attention should be paid to the presence of unexpected dynamic normal force variation during vibration-assisted friction reduction experiments, in which only a deliberate tangential or lateral excitation is applied. An uncontrolled misalignment of such excitation directions with respect to the sliding plane can lead to a time-varying normal force, eventually causing friction-induced vibrations. The combination of nonlinear contact properties along the normal direction and external excitation results in friction modulation graphs which display shapes that qualitatively resemble those obtained experimentally and are different from those derived from systems with no friction-induced oscillations.

## 6 Conclusions

In this work, the effect of external excitation and nonlinear contact properties on the stability of the steady

sliding state and on the friction modulation of a 2 degree of freedom mass on a moving belt system is studied. Both tangential and normal excitation are present and the nonlinear contact properties are represented by the Hertz-Damp model. The presence of the time-varying normal contact force and the corresponding friction friction leads to parametric excitation, triggering friction-induced oscillations. Whenever these oscillations are detected, parts of the friction force versus relative velocity plots reveal negative slopes, even though Amontons-Coulomb law is assumed. The presence of the parametrically induced negative net damping in the tangential direction is the mechanism behind friction-induced oscillations.

To predict the onset of such oscillations, a linearized stability analysis is performed taking advantage of the Method of Direct Separation of Motion that allows to incorporate the averaged effects of the friction force modulated through the applied external excitations. While the unforced system is stable at the equilibrium point, the forced system exhibits friction-induced vibration for certain regions of the parameter space. Thus, while external excitation is generally used to quench self-excited oscillation, the presence of an oscillating normal force and the normal-tangential friction coupling can also destabilise an otherwise stable equilibrium state. Additionally, the Routh-Hurwitz criterion is used to study the effect of varying the model parameters on the occurrence of friction-induced vibrations. It is found that a higher damping ratio for $\beta_1$ helps in decreasing the region where friction-induced vibrations occur. Similarly, as the natural frequency $\omega_1$ increases, the unstable region decreases, reaching its minimum near resonance. However, as $\omega_1$ continues to increase beyond this point, the unstable region expands again. For the parameter space considered, varying $\beta_2^*$ and $\omega_2^*$ has little impact on the unstable region. A higher excitation frequency $\Omega_e$ value increases the stable region. For all cases, the stability analysis does not provide information on whether the system might experience stick–slip behaviour or not. The numerical validation study demonstrated that the results from the linearized stability analysis show a good qualitative agreement with the occurrence of friction-induced oscillations, though the quantitative match varied depending on the system parameters and their values. It is worth mentioning that this study makes use of a simplified model, with reference to the investigation of parametric excitation. Modifying it could make it more representative of specific real-case scenarios, as shown in [4,10–12].

Lastly, the effect of friction-induced vibrations on friction modulation is studied. Whenever friction-induced vibration is present, the cycles in the velocity response differ from each other, since multiple oscillation frequencies are present. This results in a scatteredness in the effective friction values for the range of belt velocities for which instability is observed. Therefore, multiple effective friction values can exist for a specific belt velocity. A similar level of scatteredness can also be observed in related experimental studies. Instead, averaging over the vibration period of the tangential mode results in almost no scatteredness and in effective friction plots with shapes that qualitatively resemble those obtained experimentally or obtained using Dahl and/or Dupont models. Finally, this work calls for further experimental validation, and at the same time, it highlights the need to keep track and measure the presence of normal force oscillations that may occur during the experiments.

**Author contributions** E. Sulollari: Conceptualization, Methodology, Formal analysis, Investigation, Software, Original draft, Writing - review and editing, Visualization, Data curation. K.N. van Dalen: Methodology, Writing - review and editing, Supervision. A. Cabboi: Conceptualization, Methodology, Writing - review and editing, Supervision.

**Funding** The authors declare that no funds, grants, or other support were received during the preparation of this manuscript.

**Data availability** Data will be made available on request.

**Declarations**

**Conflict of interest** The authors declare that they have no known competing financial interests or personal relationships that could have appeared to influence the work reported in this paper.

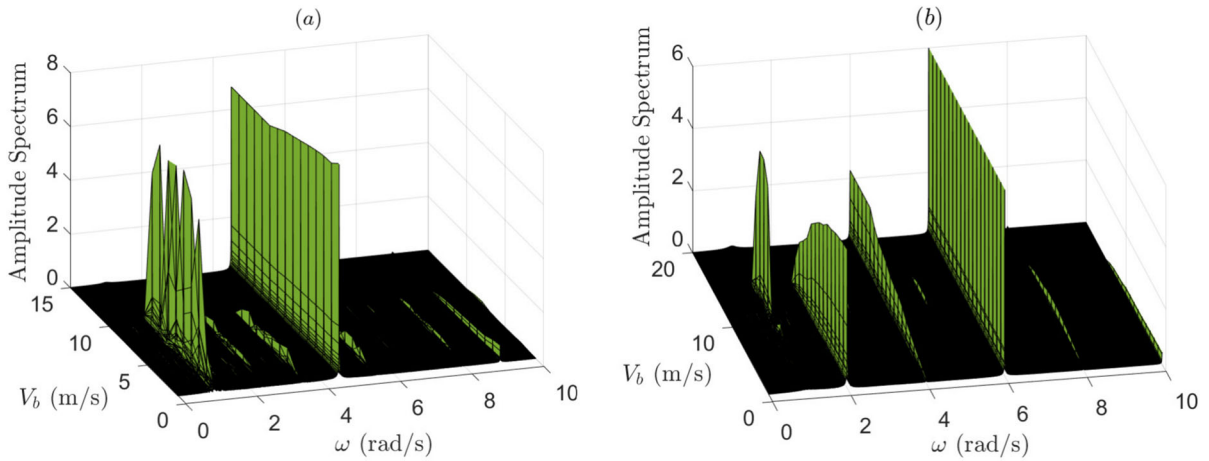


**Fig. 14** **a** Amplitude spectrum of the velocity $\dot{X}_1$ for $\Omega_e$=4.5 rad/s; **b** Amplitude spectrum of the velocity $\dot{X}_1$ for excitation frequencies 6 rad/s and 4 rad/s for the tangential and normal directions, respectively. The rest of the parameters as in Fig. 2

## Appendix A

### A.1 Numerical solution: responses for different excitation frequencies

In Sect. 3, the excitation frequency $\Omega_e$ used is an integer multiple of the natural frequency $\omega_1$. As shown in Fig. 14a, setting the excitation frequency to 4.5 rad/s still produces a noticeable spectral peak at $\omega_1$. Moreover, the spectral peak at $\omega_1$ is also evident even when the excitation frequencies applied in the tangential and normal direction differ from each other. As illustrated in Fig. 14b, when the excitation frequencies are 6 rad/s and 4 rad/s for the tangential and normal directions, respectively, the amplitude spectrum of the velocity response $\dot{X}_1$ still exhibits a notable spectral peak at $\omega_1$. The primary spectral peak aligns with the tangential excitation frequency of 6 rad/s, while the spectral peak corresponding to the normal excitation frequency of 4 rad/s is also notable. It is worth highlighting, that a strong response emerges at the second harmonic $\omega = 2\omega_1$. Hence, different excitation frequencies may induce strong higher harmonics. In comparison, the amplitudes at other harmonics are negligible.

In Fig. 15, the amplitude spectrum of the velocity response $\dot{X}_1$ is displayed for the case where the excitation in the tangential direction has a phase shift of $\pi/2$ relative to the excitation in the normal direction. The spectral peak at $\omega_1$ is again evident, meaning that friction-induced vibrations occur even when a phase shift is present. However, compared to the case of no phase shift, the velocity range for which these vibrations appear is different. Thus, the phase shift has an influence on the range of belt velocities for which friction-induced vibrations occur.

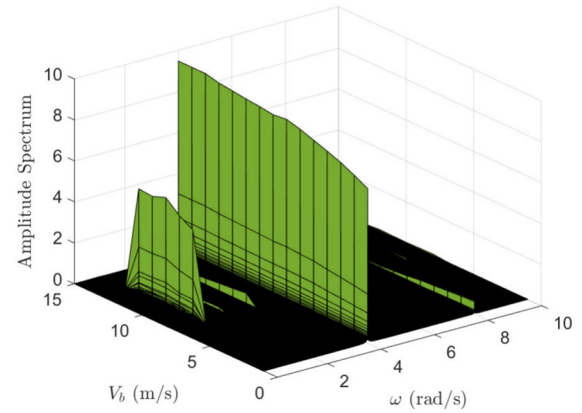


**Fig. 15** Amplitude spectrum of the velocity $\dot{X}_1$ for $\Omega_e$=4 rad/s and phase shift $\pi/2$; The rest of the parameters as in Fig. 2

### A.2 Stability analysis: Jacobian linearisation for the forced system

Here, for sake of completeness, the equations of motion $\Phi$ are obtained. As written in subsection 4.2, separating the motions $[\mathbf{X}] = [X_1\ X_2]^{\mathrm{T}}$ into the components $[\mathbf{Z}] = [Z_1\ Z_2]^{\mathrm{T}}$ and $[\Phi] = [\Phi_1\ \Phi_2]^{\mathrm{T}}$, making use of the averaging operation and subtracting the equation of motion for $\mathbf{Z}$ from the total one, the equations of

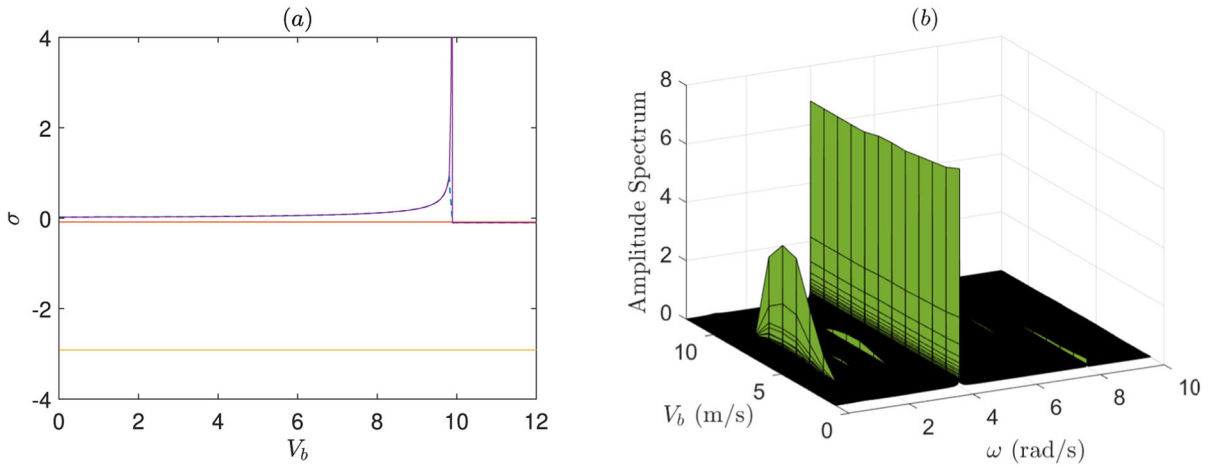


**Fig. 16** **a** Real part $\sigma$ versus $V_b$ for linear contact properties; **b** Amplitude spectrum of the velocity $\dot{X}_1$. ($\omega_1 = 1$ rad/s, $\omega_2 = 0.5$ rad/s, $\beta_1 = 0.1$, $\beta_2 = 3$, $\alpha = 2$m, $\Omega_e = 4$ rad/s and $\mu_s = 0.4$)

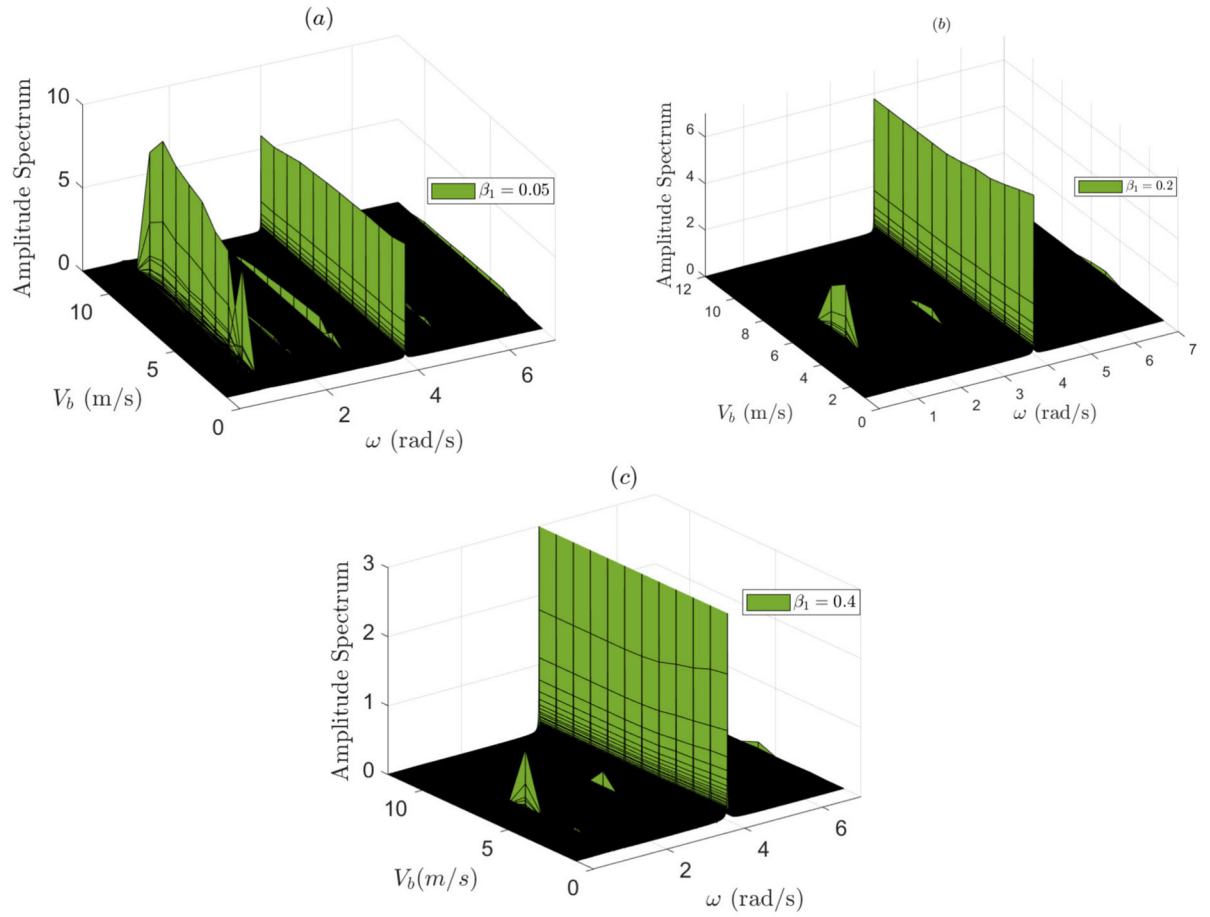


**Fig. 17** Amplitude spectrum of the velocity $\dot{X}_1$: **a** $\beta_1 = 0.05$; **b** $\beta_1 = 0.2$; (c) $\beta_1 = 0.4$. The rest of the parameters as in Fig. 2

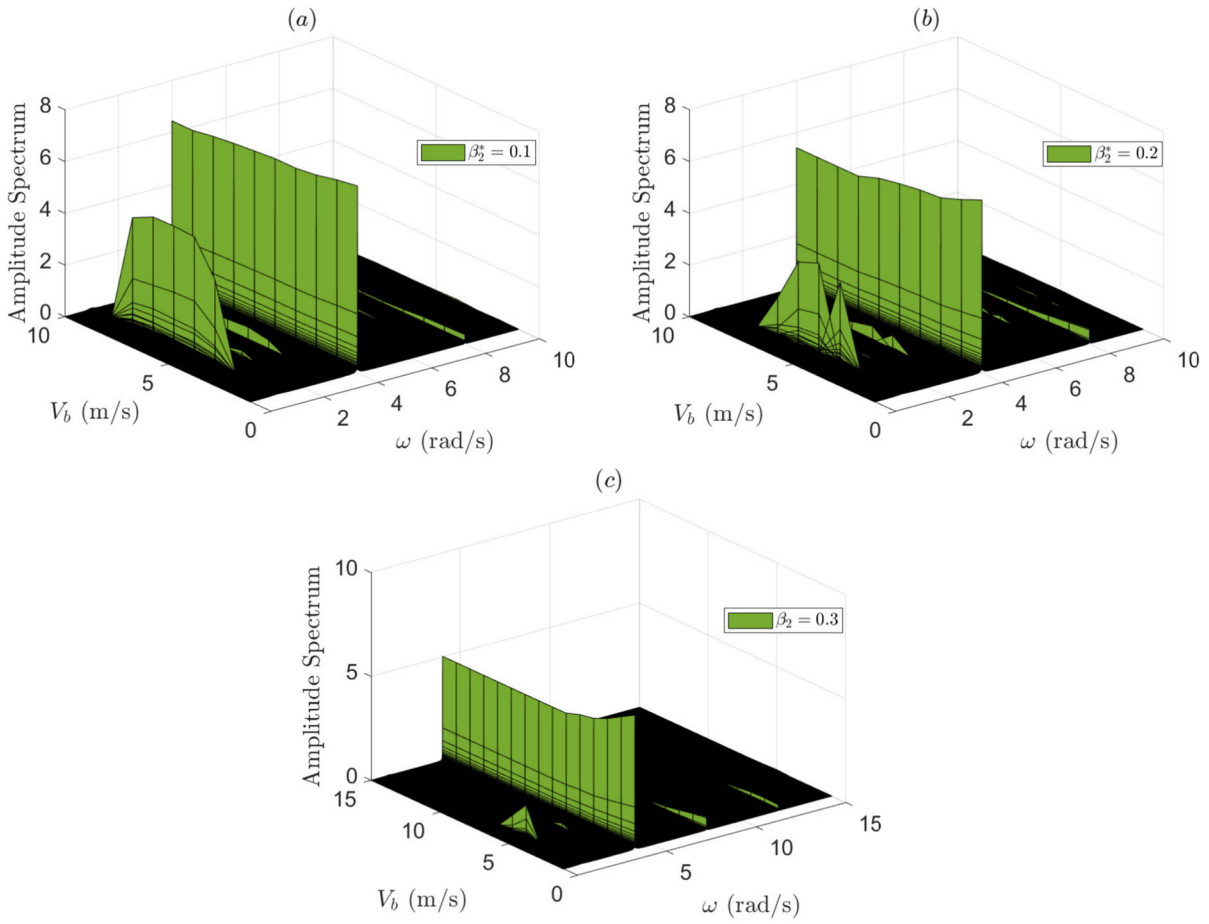


**Fig. 18** Amplitude spectrum of the velocity $\dot{X}_1$: **a** $\beta_2^* = 0.1 \frac{1}{\mathrm{m}^{5/4}}$; **b** $\beta_2^* = 0.2 \frac{1}{\mathrm{m}^{5/4}}$; **c** $\beta_2^* = 0.3 \frac{1}{\mathrm{m}^{5/4}}$. The rest of the parameters as in Fig. 2

motion for the components of $\Phi$ are obtained

$$\begin{aligned}
&\Omega_e \Phi_1'' + 2\dot{\Phi}_1' + \Omega_e^{-1}\ddot{\Phi}_1 + 2\beta_1\omega_1(\Phi_1' + \Omega_e^{-1}\dot{\Phi}_1) \\
&+\omega_1^2\Omega_e^{-1}\Phi_1 + \mu(\dot{Z}_1 - V_b + \Phi_1' + \Omega_e^{-1}\dot{\Phi}_1) \\
&\times(2\beta_2^*\omega_2^*(\dot{Z}_2 + \Phi_2' + \Omega_e^{-1}\dot{\Phi}_2) + \omega_2^{*2}) \\
&(c_3(Z_2 + \Omega_e^{-1}\Phi_2)^3 + c_2(Z_2 + \Omega_e^{-1}\Phi_2)^2 \\
&+c_1(Z_2 + \Omega_e^{-1}\Phi_2) + c_0) - \bar{\mu}(2\beta_2^*\omega_2^*\dot{Z}_2 + \omega_2^{*2}) \\
&(c_3 Z_2^3 + c_2 Z_2^2 + c_1 Z_2 + c_0) = \alpha\Omega_e^2 \sin(\Omega_e \tau)
\end{aligned} \tag{A1}$$

and

$$\begin{aligned}
&\Omega_e \Phi_2'' + 2\dot{\Phi}_2' + \Omega_e^{-1}\ddot{\Phi}_2 + (2\beta_2^*\omega_2^*(\dot{Z}_2 + \Phi_2' \\
&+\Omega_e^{-1}\dot{\Phi}_2) + \omega_2^{*2})(c_3(Z_2 + \Omega_e^{-1}\Phi_2)^3 \\
&+c_2(Z_2 + \Omega_e^{-1}\Phi_2)^2 + c_1(Z_2 + \Omega_e^{-1}\Phi_2) + c_0) \\
&-(2\beta_2^*\omega_2^*\dot{Z}_2 + \omega_2^{*2})(c_3 Z_2^3 + c_2 Z_2^2 + c_1 Z_2 + c_0) \\
&= -\alpha\Omega_e^2 \sin(\Omega_e \tau).
\end{aligned} \tag{A2}$$

In a previous work [18], it was stated that the motions can be separated for all frequencies of the excitation. Therefore, in this work, no restrictions are imposed on the order of magnitude of $\Omega_e$.

Referring again to subsection 4.2, writing the equations of slow motion, Eq. (18) and Eq. (19), in the state-space form results in

$$S_1 = \dot{Z}_1 \tag{A3}$$

$$\begin{aligned}
\dot{S}_1 = &-2\beta_1\omega_1 S_1 - \omega_1^2 Z_1 \\
&+\bar{\mu}(2\beta_2^*\omega_2^* S_2 + \omega_2^{*2}) Z_2^{3/2}
\end{aligned} \tag{A4}$$

$$S_2 = \dot{Z}_2 \tag{A5}$$

$$\dot{S}_2 = -(2\beta_2^*\omega_2^* S_2 + \omega_2^{*2}) Z_2^{3/2} + g \tag{A6}$$

Setting the Eqs. (A3)–(A6) to zero, the equilibrium points are

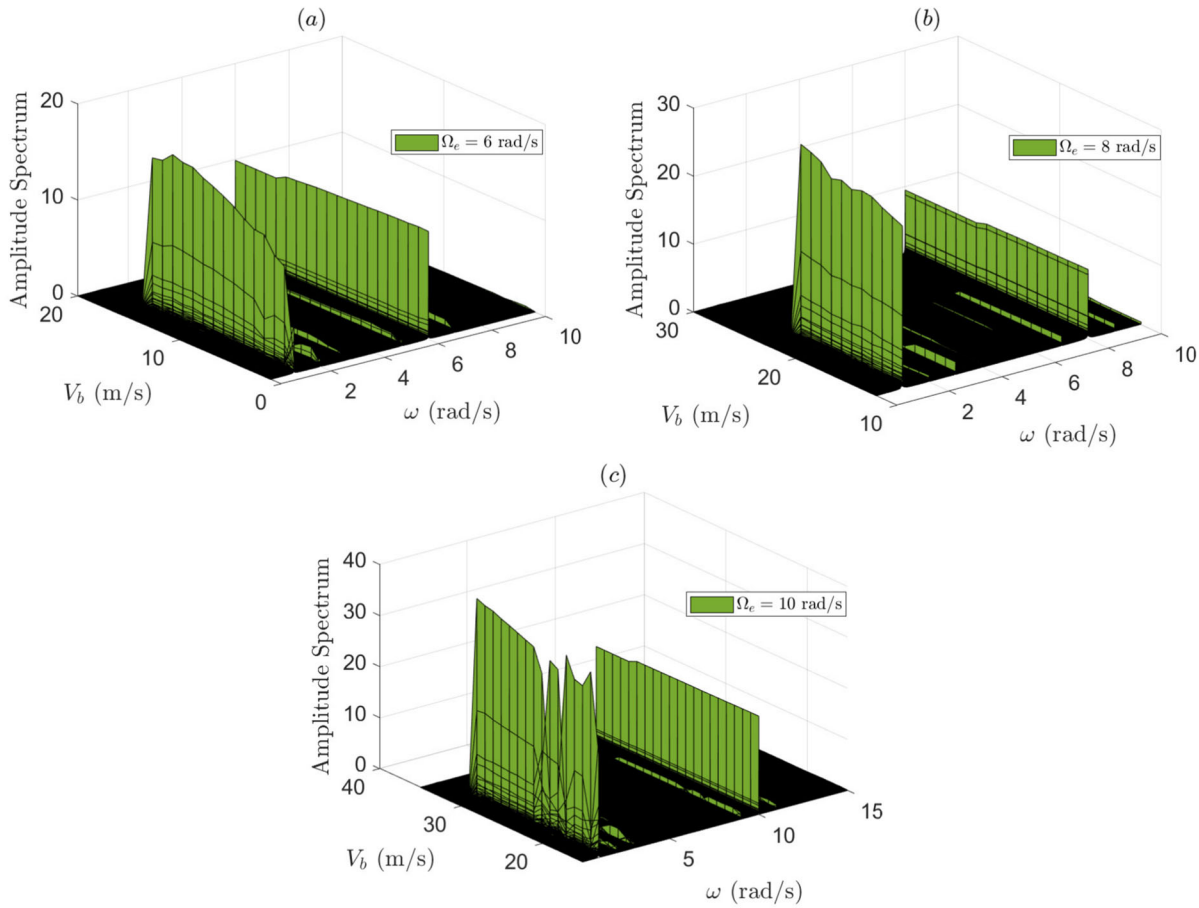


**Fig. 19** Amplitude spectrum of the velocity $\dot{X}_1$: **a** $\Omega_e = 6$ rad/s; **b** $\Omega_e = 8$ rad/s; **c** $\Omega_e = 10$ rad/s. The rest of the parameters as in Fig. 2

$$(Z_1^0, S_1^0) = \left(\frac{\bar{\mu}^0 g}{\omega_1^2}, 0\right),$$
$$(Z_2^0, S_2^0) = \left(\left(\frac{g}{\omega_2^{*2}}\right)^{2/3}, 0\right). \tag{A7}$$

### A.3 Numerical solution: linear contact properties

Referring to the discussion in subsection 4.2, here, a 2 DOF system with linear contact properties is considered, as detailed in [18]. For $\beta_2 = 3$, the system is overdamped in the normal direction and has an unstable equilibrium, as illustrated in Fig. 16a. Thus, friction-induced oscillations occur (see the peak at $\omega_1$ in the amplitude spectrum, Fig. 16b) for $V_b$ values less than the bifurcation point, $V_b \approx 10$ m/s, despite the assumption of linear contact properties. As in the case of nonlinear contact properties, the presence of a positive net damping in parts of the oscillation cycles bounds the response. In general, a better correlation (than in Fig. 2b) in the range of belt velocities between the stability analysis and the numerical results is observed, since the effective friction expression used corresponds to the system with linear contact properties.

### A.4 Routh-Hurwitz criterion: $a_1$, $a_2$, $a_3$ and $a_4$ expressions

Here, the expressions for $a_1$, $a_2$, $a_3$, and $a_4$ utilized in deriving the Routh-Hurwitz coefficients in subsection 4.3 are displayed.

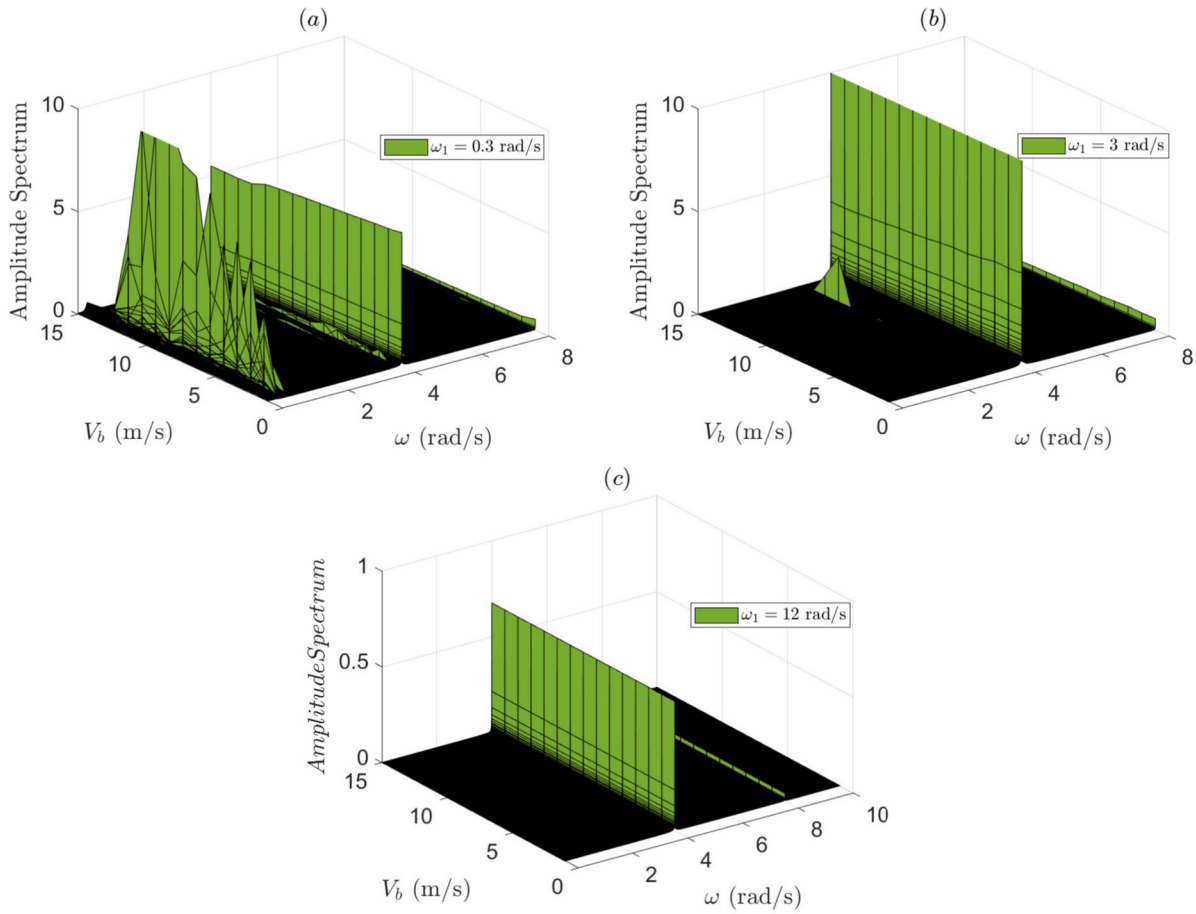


**Fig. 20** Amplitude spectrum of the velocity $\dot{X}_1$: **a** $\omega_1 = 0.3\ \frac{\text{rad}}{\text{s}}$; **b** $\omega_1 = 3\ \frac{\text{rad}}{\text{s}}$; **c** $\omega_1 = 12\ \frac{\text{rad}}{\text{s}}$. The rest of the parameters as in Fig. 2

$$
\begin{aligned}
a_1 &= 2\beta_1\omega_1 - \bar{\mu}' g + \frac{2\beta_2^* g}{\omega_2^*} \\
a_2 &= \omega_1^2 + (-2\beta_1\omega_1 + \bar{\mu}' g)\left(\frac{-2\beta_2^* g}{\omega_2^*}\right) \\
&\quad + \frac{3}{2}\omega_2^{*2}\left(\frac{g}{\omega_2^{*2}}\right)^{1/3} \\
a_3 &= \frac{2\beta_2^* g\omega_1^2}{\omega_2^*} + (-2\beta_1\omega_1 + \bar{\mu}' g) \\
&\quad \left(\frac{-3}{2}\omega_2^{*2}\left(\frac{g}{\omega_2^{*2}}\right)^{1/3}\right) \\
a_4 &= \frac{3}{2}\omega_1^2\omega_2^{*2}\left(\frac{g}{\omega_2^{*2}}\right)^{1/3}
\end{aligned}
\tag{A8}
$$

### A.5 Numerical validation of stability diagrams

Referring to the discussion in subsection 4.3, here, numerical results of the amplitude spectrum are displayed to validate parts of the stability diagrams. The stability diagram in Fig. 6a shows that a higher $\beta_1$ value helps in decreasing the range of belt velocities where friction-induced vibrations occur. The amplitude spectra in Fig. 17 show that, indeed, as $\beta_1$ value increases from 0.05 in Fig. 17a, to 0.2 in Fig. 17b and 0.4 in Fig. 17c, the range of belt velocities for which friction-induced vibrations are observed decreases.

The stability diagram of $\beta_2^*$ displayed in Fig. 6b shows that the unstable region remains relatively the same as $\beta_2^*$ values are varied. The amplitude spectra in Fig. 18 illustrate that as the value of $\beta_2^*$ increases from $0.1\frac{1}{\text{m}^{5/4}}$ in Fig. 18a to $0.2\frac{1}{\text{m}^{5/4}}$ in Fig. 18b, and further to $0.3\frac{1}{\text{m}^{5/4}}$ in Fig. 18c, the range of belt velocities for

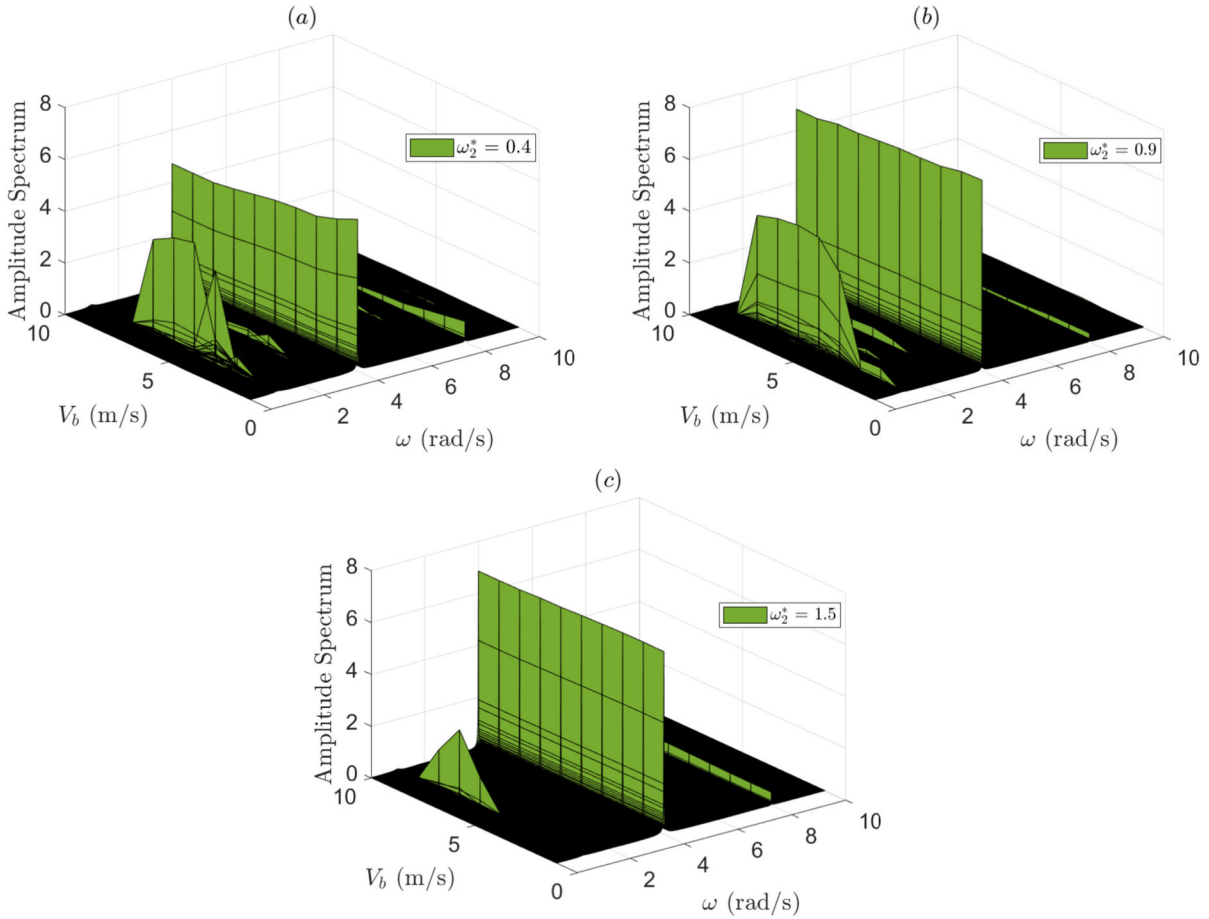


**Fig. 21** Amplitude spectrum of the velocity $\dot{X}_1$: **a** $\omega_2^* = 0.4$ $\frac{\text{rad}}{\text{m}^{1/4}\text{s}}$; **b** $\omega_2^* = 0.9$ $\frac{\text{rad}}{\text{m}^{1/4}\text{s}}$; **c** $\omega_2^* = 1.5$ $\frac{\text{rad}}{\text{m}^{1/4}\text{s}}$. The rest of the parameters as in Fig. 2

which friction-induced oscillation occur decreases. In all cases, no friction-induced vibrations are observed for $V_b > 8$ m/s, which matches the stability diagram. However the quantitative match is not good for smaller $V_b$ and high $\beta_2^*$ values, as the numerical results show a decrease in the range of belt velocities for which friction-induced oscillations are triggered.

The stability diagram of $\Omega_e$, Fig. 7, show that the instability region decreases for increased $\Omega_e$ values. Figure 19a displays the amplitude spectrum for $\Omega_e = 6$ rad/s which shows a good qualitative and quantitative match to the stability diagram. For excitation frequencies $\Omega_e = 8$ rad/s and $\Omega_e = 10$ rad/s, the numerical results indicate that stick–slip behavior occurs within the stability regions shown in the stability diagram, specifically for $V_b$ values below 10 m/s and 15 m/s, respectively. Therefore, the amplitude spectra in Fig. 19b, c start at belt velocities $V_b$ higher than these values. The numerical results also show that the stability diagram underestimates the size of the unstable region as the excitation frequencies rise, since they show friction-induced vibrations over a broader range of belt velocities.

The stability diagram in Fig. 8a shows that as $\omega_1$ value increases, the instability region decreases, reaching its minimum when $\omega_1 = \Omega_e = 4$ rad/s. The numerical results confirm that as $\omega_1$ increases from 0.3 rad/s in Fig. 20a to 3 rad/s in Fig. 20b, the range of belt velocities exhibiting friction-induced oscillations narrows. At even higher $\omega_1$ values, such as $\omega_1 = 12$ rad/s, no peak is seen in the amplitude spectrum, as shown in Fig. 20c, aligning with the stability diagram. Thus, there is good qualitative and quantitative agreement between the stability diagram and the numerical results.

Regarding the influence of $\omega_2^*$, the stability diagram in Fig. 8b shows that varying $\omega_2^*$ slightly decreases the instability region. The amplitude spectra in Fig. 21 show a good quantitative match to the stability diagram for $V_b > 8$ m/s. At lower belt velocities, the quantitative match deteriorates, as the reduction in the belt velocity ranges where friction-induced oscillations occur is more pronounced in the numerical results. This indicates that the stability diagrams overestimate the extent of the unstable region.

## References


1. Ibrahim, R.A.: Friction-induced vibration chatter squeal and chaos. Part II: dynamics and modeling. Appl. Mech. Rev. **47**(7), 227–253 (1994)
2. Spurr, R.T.: A theory of brake squeal. Proc. Automob. Div. Inst. Mech. Eng **15**(1), 33–52 (1961)
3. Hoffmann, N., Gaul, L.: A sufficient criterion for the onset of sprag-slip oscillations. Arch. Appl. Mech. **73**(9–10), 650–660 (2004)
4. Sinou, J.-J., Dereure, O., Mazet, G.-B., Thouverez, F., Jezequel, L.: Friction-induced vibration for an aircraft brake systemâ€"part 1: Experimental approach and stability analysis. Int. J. Mech. Sci. **48**(5), 536–554 (2006)
5. Hoffmann, N., Gaul, L.: Effects of damping on mode-coupling instability in friction induced oscillations. J. Appl Math Mech-Engl **83**, 524–534 (2003)
6. Sinou, J., Jezequel, L.: Mode coupling instability in friction-induced vibrations and its dependency on system parameters including damping. Eur. J. Mech. A/Solids **26**, 106–122 (2007)
7. Li, Z., Ouyang, H., Guan, Z.: Nonlinear friction-induced vibration of a slider-belt system. J. Vib. Acoust. **138**, 041006 (2016)
8. Li, Z., Ouyang, H., Wei, Z.-H.: Insights into instability of friction-induced vibration of multi-degree-of-freedom models. J. Sound Vib. **503**, 116107 (2021)
9. Bigoni, D., Kirillov, O.N., Misseroni, D., Noselli, G., Tommasini, M.: Flutter and divergence instability in the pflüger column: experimental evidence of the Ziegler destabilization paradox. J. Mech. Phys. Solids **116**, 99–116 (2018)
10. Massi, F., Giannini, O.: Slight effect of damping on the propensity of squeal instability: an experimental investigation. J. Acoust. Soc. Am. **123**(4), 2017–2023 (2008)
11. Fritz, G., Sinou, J.-J., Duffal, J.-M., Jézéquel, L.: Effects of damping on brake squeal coalescence patterns-application on a finite element model. Mech. Res. Commun. **34**(2), 181–190 (2007)
12. Charroyer, L., Chiello, O., Sinou, J.-J.: Parametric study of the mode coupling instability for a simple system with planar or rectilinear friction. J. Sound Vib. **384**, 94–112 (2016)
13. Thomsen, J.J.: Using fast vibrations to quench friction-induced oscillations. J. Sound Vib. **228**(5), 1079–1102 (1999)
14. Hoffmann, N., Wagner, N., Gaul, L.: Quenching mode-coupling friction-induced instability using high-frequency dither. J. Sound Vib. **279**(1), 471–480 (2005)
15. Michaux, M.A., Ferri, A.A., Cunefare, K.A.: Effect of tangential dither signal on friction induced oscillations in an sdof model. J. Comput. Nonlinear Dyn. **2**, 201–210 (2007)
16. Berger, E.J., Krousgrill, C.M., Sadeghi, F.: Stability of sliding in a system excited by a rough moving surfaces. J. Tribol. **119**(4), 672–680 (1997)
17. Berger, E.J., Krousgrill, C.M., Sadeghi, F.: Friction-induced sliding instability in a multi-degree-of-freedom system with oscillatory normal forces. J. Sound Vib. **266**(2), 369–387 (2003)
18. Sulollari, E., Dalen, K.N., Cabboi, A.: Vibration-induced friction modulation for a general frequency of excitation. J. Sound Vib. **573**, 118200 (2024)
19. Tolstoi, D.M.: Significance of the normal degree of freedom and natural normal vibrations in contact friction. Wear **10**(3), 199–213 (1967)
20. Tworzydlo, W.W., Becker, E.: Influence of forced vibrations on the static coefficient of friction â€" numerical modeling. Wear **143**(1), 175–196 (1991)
21. Matunaga, S., Onoda, J.: New gravity compensation method by dither for low-g simulation. J. Spacecr. Rockets **32**, 364–369 (1995)
22. Kapelke, S., Seemann, W.: On the effect of longitudinal vibrations on dry friction: Modelling aspects and experimental investigations. Tribol. Lett. (2018)
23. Dupont, P., Hayward, V., Armstrong, B., Altpeter, F.: Single state elastoplastic friction models. IEEE Trans. Automat. **47**(5), 787–792 (2002)
24. Leus, M., Gutowski, P., Rybkiewicz, M.: Effectiveness of friction force reduction in sliding motion depending on the frequency of longitudinal tangential vibrations, sliding velocity and normal pressure. Acta Mech. Automat. **17**(4), 490–498 (2023)
25. Leus, M., Gutowski, P., Bachtiak-Radka, E.: The effect of contact compliance of sliding pair on friction force reduction at longitudinal tangential vibrations. Tribol. Int. **187**, 108701 (2023)
26. Hunt, K.H., Crossley, F.R.E.: Coefficient of restitution interpreted as damping in vibroimpact. J. Appl. Mech. **42**(2), 440–445 (1975)
27. Blekhman, I.I.: Vibrational mechanics – nonlinear dynamic effects, general approach, applications, 4th ed. edn. World Scientific, Singaopre (2000)
28. Blekhman, I.I., Sorokin, V.S.: Effects produced by oscillations applied to nonlinear dynamic systems: a general approach and examples. Nonlinear Dyn. **83**(4), 2125–2141 (2016)
29. Hertz, H.: On the contact of elastic solids. Miscellaneous Papers, Chapter V, 146–162 (1896)
30. Cattaneo, C.: Sul contatto di due corpi elastici: distribuzione locale degli sforzi. Recond. Dell Accad. Naz. Lincei **27**, 342–248434436474478 (1938)
31. Dahl, R.P.: Solid friction damping of mechanical vibrations. AIAA J. **14**(12), 1675–1682 (1976)
32. Amontons, G.: De la resistance cause'e dans les machines (about resistance and force in machines). Mem l'Acedemie R A, 257–282 (1699)

33. Coulomb, C.A.: Theorie des Machines Simple (Theory of Simple Machines). Bachelier, Paris (1821)
34. Bryant, M.D.: Non-linear forced oscillation of a beam coupled to an actuator via Hertzian contact. J. Sound Vib. **99**, 403–414 (1985)
35. Hess, D.P., Soom, A.: Normal vibrations and friction under harmonic loads: Part I-Hertzian contacts. J. Tribol. **113**(1), 80–86 (1991)
36. Gutowski, P., Leus, M.: The effect of longitudinal tangential vibrations on friction and driving forces in sliding motion. Tribol. Int. **55**, 108–118 (2012)
37. Gutowski, P., Leus, M.: Computational model for friction force estimation in sliding motion at transverse tangential vibrations of elastic contact support. Tribol. Int. **90**, 455–462 (2015)
38. Wang, P., Ni, H., Wang, R., Li, Z., Wang, Y.: Experimental investigation of the effect of in-plane vibrations on friction for different materials. Tribol. Int. **99**, 237–247 (2016)
39. Wang, P., Ni, H., Wang, R., Liu, W., Lu, S.: Research on the mechanism of in-plane vibration on friction reduction. J. Mater. **10**(9), 1015 (2017)